Inorg. Chem. **2005**, *44*, 1794–1809

Combined Spectroscopic/Computational Study of Binuclear Fe(I)–Fe(I) Complexes: Implications for the Fully-Reduced Active-Site Cluster of Fe-Only Hydrogenases

Adam T. Fiedler and Thomas C. Brunold*

University of Wisconsin-Madison, Department of Chemistry, 1101 West University Avenue, Madison, Wisconsin 53706

Received September 8, 2004

The Fe(I)–Fe(I) dimer complex $[Fe_2(pdt)(CO)_4(CN)_2][Et_4N]_2$ (**2**), where pdt = 1,3-propane dithiolate, serves as a model of the fully reduced $[2Fe]_H$ component of the H cluster, which is the active site for catalysis in Fe-only hydrogenases (FeHases). Electronic absorption, magnetic circular dichroism (MCD), and resonance Raman (rR) spectroscopies have been employed to characterize both the ground and excited states of **2** as well as those of the related complex $Fe_2(pdt)(CO)_6$ (**1**). These results have been combined with density functional theory (DFT) computations to produce experimentally validated bonding descriptions of **1** and **2**. It is shown that Fe(I)–S covalency is significantly reduced upon dicyano substitution (i.e., conversion of **1** → **2**), while the corresponding Fe(I)–CO/CN π-backbonding interactions are strengthened, results that are corroborated by normal-coordinate analyses of the vibrational data. Detailed assignments of the features observed in the electronic absorption spectra of **1** and **2** have been developed on the basis of time-dependent DFT (TD-DFT) calculations, which provide remarkably accurate simulations of the experimental data. For both complexes, all bands below 32 000 cm^{-1} arise from transitions involving electronic excitation within the binuclear Fe–Fe core, with the most intense feature assigned to the Fe(σ^b) → Fe(σ^*) transition. Analysis of the corresponding rR excitation profiles within the framework of time-dependent Heller theory reveals that in each case the Fe–Fe bond is elongated by ~0.3 Å in the Fe(σ^b) → Fe(σ^*) excited state. Finally, building upon the insights gained from the spectroscopic/computational studies of **1** and **2**, our computational methodology has been extended to the reduced enzyme active site, providing insights into the electronic structure of the $[2Fe]_H$ subcluster in the $\mathbf{H_{red}}$ state and its relationship to catalysis.

Introduction

Molecular hydrogen plays an important role in the metabolism of numerous aerobic and anaerobic microorganisms. Central to the biological utilization of H_2 is a family of enzymes known as hydrogenases that catalyze the reversible reaction $H_2 \leftrightarrows 2H^+ + 2e^-$.[1,2] Although all hydrogenases contain multiple "conventional" $[Fe_2S_2]$ and $[Fe_4S_4]$ clusters, the site of hydrogen activation in Fe-only hydrogenases (FeHases) is an unusual Fe−S cluster known as the H cluster (Scheme 1), which consists of a $[Fe_4S_4]$ cubane linked to a 2Fe subcluster (often referred to as the $[2Fe]_H$ component).[3,4]

Scheme 1. FeHase H Cluster Structure

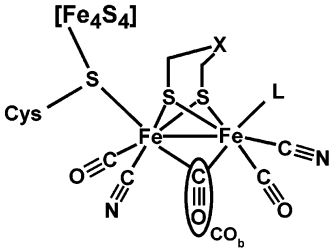

X = CH_2 (pdt) or NH (dta)
L = vacant, H_2O, CO, H_2, or H

Each Fe atom within this subcluster is coordinated by a terminal CN and CO ligand,[4] and the two metal centers are

* Author to whom correspondence should be addressed. E-mail: brunold@chem.wisc.edu.

(1) (a) Armstrong, F. A. *Curr. Opin. Chem. Biol.* **2004**, *8*, 133−140. (b) Adams, M. W. W.; Stiefel, E. I. *Curr. Opin. Chem. Biol.* **2000**, *4*, 214−220.
(2) Evans, D. J.; Pickett, C. J. *Chem. Soc. Rev.* **2003**, *32*, 268−275.
(3) Peters, J. W.; Lanzilotta, W. N.; Lemon, B. J.; Seefeldt, L. C. *Science* **1998**, *282*, 1853−1858.
(4) Nicolet, Y.; Piras, C.; Legrand, P.; Hatchikian, C. E.; Fontecilla-Camps, J. C. *Structure* **1999**, *7*, 13−23.

10.1021/ic048739n CCC: $30.25
Published on Web 02/10/2005

bridged by an exogenous dithiolate ligand presumed to be either a propanedithiolate (pdt) or di(thiomethyl)amine (dta) (X = CH_2 or NH, respectively, in Scheme 1).[5,6] An additional CO ligand (CO_b) occupies a position between the Fe centers with its binding mode (bridging versus terminal) depending upon the oxidation state of the cluster.[6] The coordination sphere of the proximal Fe (Fe_p) is completed by a cysteine linkage to the [Fe_4S_4] cubane, while the distal Fe (Fe_d) has a labile coordination site (L) that is the putative site of H_2 binding and catalysis. Overall, the organometallic nature of the 2Fe subcluster is quite intriguing, as strong-field ligands such as CO and CN are rarely found in biological systems. Moreover, the short Fe−Fe distance of 2.6 Å in the $[2Fe]_H$ component suggests the presence of an unusually strong metal−metal bond for a biological system.[4]

Spectroscopic studies of FeHases have revealed that the $[2Fe]_H$ component of the H cluster exists in several oxidation states. The as-isolated form of FeHase from *Desulfovibrio vulgaris* is inactive and EPR silent when the enzyme is purified in air.[7] Reductive activation of the enzyme generates the $\mathbf{H_{ox}}$ state, which is active and paramagnetic. Conversely, the hydrogenase from *Clostridium pasteurianum* is unstable toward purification in air; when purified anaerobically, it is isolated with the H cluster already in the $\mathbf{H_{ox}}$ state, exhibiting the "rhombic 2.10" EPR signal.[8−10] FeHases are strongly inhibited by CO, and incubation of the $\mathbf{H_{ox}}$ state with CO gives rise to the appearance of the "axial 2.07" EPR signal.[9,11] Finally, treatment of FeHases with dithionite produces the EPR-silent $\mathbf{H_{red}}$ state.[12] FTIR and crystallographic studies have shown that the bridging carbonyl in the $\mathbf{H_{red}}$ state is shifted toward Fe_d, resulting in a terminal CO_b ligand.[6] Although it has been a matter of dispute, computational results suggest that the $[2Fe]_H$ component cycles between the Fe(II)−Fe(II) and Fe(I)−Fe(I) oxidation states during FeHase catalysis.[13] Interestingly, Mössbauer studies have indicated that the [Fe_4S_4] cubane remains in the +2 (oxidized) state in all well-characterized forms of the H cluster.[14]

The unique structure of the H cluster has prompted several inorganic chemists to synthesize models of the $[2Fe]_H$ component. Conveniently, this structural fragment bears a close resemblance to a series of Fe(I)−Fe(I) dimers with the general formula $Fe_2(SR)_2(CO)_4(X)_2$ that have been studied extensively for decades (X = CO or phosphine ligand).[15] In 1999, several groups made this chemistry relevant to FeHases by replacing two of the carbonyl ligands of $Fe_2(pdt)(CO)_6$ (**1**) with CN to yield $[Fe_2(pdt)(CO)_4(CN)_2][Et_4N]_2$ (**2**) (Scheme 2, pdt = 1,3-propane dithiolate), providing a reasonable model of the $\mathbf{H_{red}}$ state.[16−18] Like the $[2Fe]_H$ component, complex **2** has one CN ligand on each Fe atom, and the Fe−Fe bond distance of 2.52 Å is indicative of strong metal−metal bonding.[16] Significantly, it has been shown that close analogues of **2**, such as $Fe_2(pdt)(CO)_4(CN)(PMe_3)^{1-}$ (**3**), are capable of catalyzing H_2 production in acidic electrochemical cells, demonstrating that these dimers may serve as both structural *and* functional models of the H cluster.[19] Rauchfuss and co-workers determined that the catalytic cycle of this model involves an Fe(II)−Fe(II) species with a bridging hydride ligand, $Fe_2(H)(pdt)(CO)_4(CN)(PMe_3)$ (**4**), which can be isolated in good yield (Scheme 2). Darensbourg and co-workers also explored the functional properties of FeHase model complexes, finding that complexes related to **4** are capable of catalyzing H/D exchange when exposed to sunlight.[20]

Although the synthetic FeHase models shown in Scheme 2 have been the focus of several theoretical studies,[13,21,22] there exist comparatively few studies that have probed their

Scheme 2. Synthetic Models of $[2Fe]_H$ Subcluster[16−19]

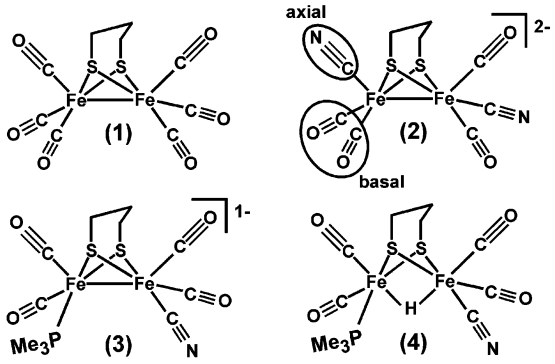

(5) (a) De Lacey, A. L.; Stadler, C.; Cavazza, C.; Hatchikian, E. C.; Fernandez, V. M. *J. Am. Chem. Soc.* **2000**, *122*, 11232−11233. (b) Pierik, A. J.; Hulstein, M.; Hagen, W. R.; Albracht, S. P. J. *Eur. J. Biochem.* **1998**, *258*, 572−578.
(6) Nicolet, Y.; de Lacey, A. L.; Vernede, X.; Fernandez, V. M.; Hatchikian, E. C.; Fontecilla-Camps, J. C. *J. Am. Chem. Soc.* **2001**, *123*, 1596−1601.
(7) Pierik, A. J.; Hagen, W. R.; Redeker, J. S.; Wolbert, R. B. G.; Boersma, M.; Verhagen, M.; Grande, H. J.; Veeger, C.; Mutsaers, P. H. A.; Sands, R. H.; Dunham, W. R. *Eur. J. Biochem.* **1992**, *209*, 63−72.
(8) Zambrano, I. C.; Kowal, A. T.; Mortenson, L. E.; Adams, M. W. W.; Johnson, M. K. *J. Biol. Chem.* **1989**, *264*, 20974−20983.
(9) Adams, M. W. W. *J. Biol. Chem.* **1987**, *262*, 15054−15061.
(10) Adams, M. W. W.; Mortenson, L. E. *J. Biol. Chem.* **1984**, *259*, 7045−7055.
(11) (a) Bennett, B.; Lemon, B. J.; Peters, J. W. *Biochemistry* **2000**, *39*, 7455−7460. (b) Lemon, B. J.; Peters, J. W. *J. Am. Chem. Soc.* **2000**, *122*, 3793−3794. (c) Kowal, A. T.; Adams, M. W. W.; Johnson, M. K. *J. Biol. Chem.* **1989**, *264*, 4342−4348.
(12) Rusnak, F. M.; Adams, M. W. W.; Mortenson, L. E.; Munck, E. *J. Biol. Chem.* **1987**, *262*, 38−41.
(13) Cao, Z. X.; Hall, M. B. *J. Am. Chem. Soc.* **2001**, *123*, 3734−3742.
(14) (a) Pereira, A. S.; Tavares, P.; Moura, I.; Moura, J. J. G.; Huynh, B. H. *J. Am. Chem. Soc.* **2001**, *123*, 2771−2782. (b) Popescu, C. V.; Munck, E. *J. Am. Chem. Soc.* **1999**, *121*, 7877−7884.
(15) (a) Leborgne, G.; Grandjean, D.; Mathieu, R.; Poilblanc, R. *J. Organomet. Chem.* **1977**, *131*, 429−438. (b) Dahl, L. F.; Wei, C.-H. *Inorg. Chem.* **1963**, *2*, 328−333. (c) Hieber, W.; Spacu, P. *Z. Anorg. Allg. Chem.* **1937**, *233*, 353−364. (d) Seyferth, D.; Henderson, R. S.; Song, L. C. *Organometallics* **1982**, *1*, 125−133.
(16) Schmidt, M.; Contakes, S. M.; Rauchfuss, T. B. *J. Am. Chem. Soc.* **1999**, *121*, 9736−9737.
(17) Lyon, E. J.; Georgakaki, I. P.; Reibenspies, J. H.; Darensbourg, M. Y. *Angew. Chem., Int. Ed.* **1999**, *38*, 3178−3180.
(18) Le Cloirec, A.; Best, S. P.; Borg, S.; Davies, S. C.; Evans, D. J.; Hughes, D. L.; Pickett, C. J. *Chem. Commun.* **1999**, 2285−2286.
(19) (a) Gloaguen, F.; Lawrence, J. D.; Rauchfuss, T. B.; Benard, M.; Rohmer, M. M. *Inorg. Chem.* **2002**, *41*, 6573−6582. (b) Gloaguen, F.; Lawrence, J. D.; Rauchfuss, T. B. *J. Am. Chem. Soc.* **2001**, *123*, 9476−9477.
(20) (a) Zhao, X.; Georgakaki, I. P.; Miller, M. L.; Mejia-Rodriguez, R.; Chiang, C. Y.; Darensbourg, M. Y. *Inorg. Chem.* **2002**, *41*, 3917−3928. (b) Zhao, X.; Georgakaki, I. P.; Miller, M. L.; Yarbrough, J. C.; Darensbourg, M. Y. *J. Am. Chem. Soc.* **2001**, *123*, 9710−9711.
(21) Georgakaki, I. P.; Thomson, L. M.; Lyon, E. J.; Hall, M. B.; Darensbourg, M. Y. *Coord. Chem. Rev.* **2003**, *238*, 255−266.
(22) Bruschi, M.; Fantucci, P.; De Gioia, L. *Inorg. Chem.* **2002**, *41*, 1421−1429.

electronic structures by using experimental methods.[23] We have examined complexes **1** and **2** using electronic absorption, magnetic circular dichroism (MCD), and resonance Raman (rR) spectroscopies, in conjunction with density functional theory (DFT) and time-dependent DFT (TD-DFT) calculations. Our objectives in undertaking such studies were multiple. First, the combination of spectroscopic and computational techniques allows for the generation of experimentally validated electronic structure descriptions of the ground and excited states of **1** and **2**. These results then provide a useful starting point for a more complete understanding of the electronic structure of the H cluster itself. Furthermore, well-defined H cluster models provide ideal systems for testing the accuracy of advanced DFT methods. TD-DFT, which provides calculated absorption and circular dichroism spectra, has primarily been applied to organic molecules or transition-metal complexes with ligand-based electronic transitions[24] and has rarely been used to simulate the metal-based transitions of polynuclear systems.[25] In this work, we have applied the TD-DFT method to complexes **1** and **2** to gauge its ability to predict the electronic absorption spectra of Fe(I) dimers and, by extension, of the reduced $[2Fe]_H$ component of the H cluster. Finally, it is worth noting that, aside from their relevance to FeHases, these models exhibit interesting spectroscopic features that are worthy of study in their own right. In particular, analysis of the unusual resonance de-enhancement observed in the rR excitation profiles of both **1** and **2** has allowed us to probe the excited-state geometries of these complexes. Collectively, our experimental and computational results obtained for complexes **1** and **2** provide significant insights into the bonding and electronic structures of these H cluster models. The implications of these results for the FeHase active site are explored by applying the same computational approach to the $\mathbf{H_{red}}$ state of the H cluster.

Experimental Section

Complex Synthesis. All reagents were purchased from Aldrich and used as obtained. Complexes **1**[26] and **2**[27] were synthesized and characterized according to published procedures. The synthesis of **2** with ^{13}C-labeled cyano ligands was accomplished with minor modifications to the procedure reported by Rauchfuss and co-workers.[27] Specifically, to a solution of **1** in MeCN was added 2 equiv of K(^{13}CN) dissolved in MeOH. The mixture was stirred at room temperature, and the progress of the reaction was monitored with IR spectroscopy. When the reaction was complete, 2 equiv of $[Et_4N]Br$ was added, and the solvent was removed under vacuum. Note that the coproduct formed in this process, KBr, does not spectrally interfere with the vibrational features associated with **2** and was thus not removed from the final product. The incorporation of ^{13}CN into the final product was confirmed by IR spectroscopy, as well as relative peak intensities in the ^{13}C NMR spectrum. IR (MeCN): $\nu_{CN} = 2029$ cm^{-1}; $\nu_{CO} = 1965$, 1921, and 1885 cm^{-1}. The electronic absorption and ^{1}H NMR spectra of the labeled complex are identical to those published previously for the natural abundance complex.

Spectroscopy. Infrared spectra were measured using a Polaris FT-IR spectrometer manufactured by Mattson Instruments, and ^{1}H and ^{13}C NMR spectra were acquired on a Bruker AC-300 spectrometer. Room-temperature absorption spectra were collected with a Varian Cary 5E UV−vis−NIR spectrophotometer. Low-temperature (77 K) electronic absorption and MCD spectra were obtained using a Jasco J-715 spectropolarimeter in conjunction with an Oxford Instruments SM-4000 8T magnetocryostat. The samples used for low-temperature experiments were prepared in a 1:1 solvent mixture of propionitrile and butyronitrile to ensure glass formation upon freezing. All MCD spectra reported herein were obtained by subtracting the −7 T spectrum from the +7 T spectrum to eliminate CD contributions.

Resonance Raman (rR) spectra were obtained upon excitation with a Coherent I-305 Ar^+ laser (between 514 and 458 nm) and a Coherent I-302C Kr^+ laser (between 657 and 521 nm) with ∼10−35 mW of laser power at the sample. The scattered light was collected using an ∼135° backscattering arrangement, dispersed by an Acton Research triple monochromator equipped with 1200 grooves/mm gratings, and analyzed with a Princeton Instruments Spec X 100BR deep-depletion, back-thinned CCD camera. Solid-state samples were prepared by thoroughly mixing ∼10 mg of the sample with ∼30 mg of KBr (a small amount of K_2SO_4 was added to some samples as an internal reference). Solution samples were prepared in degassed MeCN with concentrations ranging from 3 to 5 mM. As complex **2** is air sensitive, all sample preparation was performed in a glovebox. Spectra were accumulated at 77 K by placing the sample (contained in an NMR tube) in an EPR dewar filled with liquid N_2 to prevent sample degradation during data collection. rR excitation profiles were measured by quantifying the peak intensities relative to that of the 390 cm^{-1} solvent peak of frozen MeCN. All points in the rR excitation profiles represent the average of at least three data sets, where the error bars indicate the standard deviation of these points at each excitation wavelength.

Data Analysis. Normal-coordinate analysis (NCA) calculations used a general valence force field and were performed using the QCPE program 576 developed by Peterson and McIntosh, which solves the vibrational secular equation $\mathbf{GFL} = \lambda\mathbf{L}$. Simulations of the absorption spectra and rR excitation profiles were carried out using the time-dependent theory of electronic spectroscopy formulated by Heller and co-workers,[28,29] which we implemented in a Mathcad script. A damping factor of $\Gamma = 600$ cm^{-1}, which is appropriate for transition-metal systems,[28] was used to account for both homogeneous and inhomogeneous line broadening.

(23) A rare example of a spectroscopic/electronic-structure study of FeHase model complexes is: Yang, X.; Razavet, M.; Wang, X. B.; Pickett, C. J.; Wang, L. S. *J. Phys. Chem. A* **2003**, *107*, 4612−4618.

(24) Our previous studies involving TD-DFT are described in the following references: (a) Brooks, A. J.; Vlasie, M.; Banerjee, R.; Brunold, T. C. *J. Am. Chem. Soc.* **2004**, *126*, 8167−8180. (b) Stich, T. A.; Brooks, A. J.; Buan, N. R.; Brunold, T. C. *J. Am. Chem. Soc.* **2003**, *125*, 5897−5914. (c) Stich, T. A.; Buan, N. R.; Brunold, T. C. *J. Am. Chem. Soc.* **2004**, *126*, 9735−9749. (d) Craft, J. L.; Horng, Y. C.; Ragsdale, S. W.; Brunold, T. C. *J. Am. Chem. Soc.* **2004**, *126*, 4068−4069. (e) Craft, J. L.; Horng, Y. C.; Ragsdale, S. W.; Brunold, T. C. *J. Biol. Inorg. Chem.* **2004**, *9*, 77−89.

(25) For examples of TD-DFT applied to polynuclear transition-metal clusters, see the following references: (a) Ebihara, M.; Iiba, M.; Higashi, S.; Tsuzuki, N.; Kawamura, T.; Morioka, T.; Ozawa, S.; Yamabe, T.; Masuda, H. *Polyhedron* **2003**, *22*, 3413−3422. (b) Wu, D. Y.; Hayashi, M.; Chang, C. H.; Liang, K. K.; Lin, S. H. *J. Chem. Phys.* **2003**, *118*, 4073−4085. (c) Bakker, M. J.; Vergeer, F. W.; Hartl, F.; Rosa, P.; Ricard, L.; Le Floch, P.; Calhorda, M. J. *Chem.—Eur. J.* **2002**, *8*, 1741−1752.

(26) Lyon, E. J.; Georgakaki, I. P.; Reibenspies, J. H.; Darensbourg, M. Y. *J. Am. Chem. Soc.* **2001**, *123*, 3268−3278.

(27) Gloaguen, F.; Lawrence, J. D.; Schmidt, M.; Wilson, S. R.; Rauchfuss, T. B. *J. Am. Chem. Soc.* **2001**, *123*, 12518−12527.

(28) Zink, J. I.; Shin, K. S. K. *Adv. Photochem.* **1991**, *16*, 119.

(29) Tannor, D. J.; Heller, E. J. *J. Chem. Phys.* **1982**, *77*, 202−218.

Computations. (a) Computational Models. For complexes **1** and **2**, the computational models used in most DFT calculations were based entirely on the corresponding X-ray crystal structures[16,17] and included all atoms except for the counteranions. Yet to test the validity of our computational methods, we also performed geometry optimizations of **1** and **2** with the Amsterdam Density Functional (ADF) 2002.03 software package,[30] yielding models $\mathbf{1^{opt}}$ and $\mathbf{2^{opt}}$. These optimizations were carried out on a cluster of 20 Intel Xeon processors (Ace computers) using ADF basis set IV (triple-ζ with single polarization on the ligand atoms), an integration constant of 4.0, and the Vosko−Wilk−Nusair local density approximation[31] with the nonlocal gradient corrections of Becke[32] and Perdew.[33] The same methodology was applied to the $[2Fe]_H$ subcluster in the $\mathbf{H_{red}}$ state, and the initial atomic positions for these $\mathbf{H_{red}}$ models were derived from the crystallographic study of fully reduced FeHase from *D. desulfuricans*.[6] The Cartesian coordinates for the DFT geometry-optimized models $\mathbf{1^{opt}}$, $\mathbf{2^{opt}}$, $\mathbf{[2Fe]_H}$**-S**, and $\mathbf{[2Fe]_H}$**-SH** are available in the Supporting Information (Tables S5 and S6).

(b) Single-Point DFT and TD-DFT Calculations. All single-point DFT calculations were performed using the ORCA 2.2 software package developed by Dr. F. Neese.[34] The computations were carried out within a spin-restricted formalism, using Ahlrich's valence triple-ζ basis set[35] with one set of polarization functions[36] on all atoms, along with the corresponding auxiliary basis set (VTZ/J).[37] The calculations employed Becke's three-parameter hybrid functional[38] for exchange along with the Lee−Yang−Parr correlation functional (B3LYP)[39] with an integration grid of 4.0. The gOpenMol program[40] developed by Laaksonen was used to generate isosurface plots of molecular orbitals (using an isodensity value of 0.05 au).

Transition energies and dipole moments for all models were calculated with the TD-DFT method[41] within the Tamm−Dancoff approximation[42] as implemented in ORCA 2.2.[34] These calculations employed the hybrid B3LYP functional along with the basis sets described above. Convergence of the TD-DFT calculations required that the resolution of the identity approximation be used in calculating the Coulomb term.[43] In each case, at least 40 excited states were calculated. To aid in the interpretation and assignment of transitions, changes in electron density distribution upon excitation were evaluated by computing electron density difference maps (EDDMs). These maps were visualized with the gOpenMol program[40] using an isodensity value of 0.003 au.

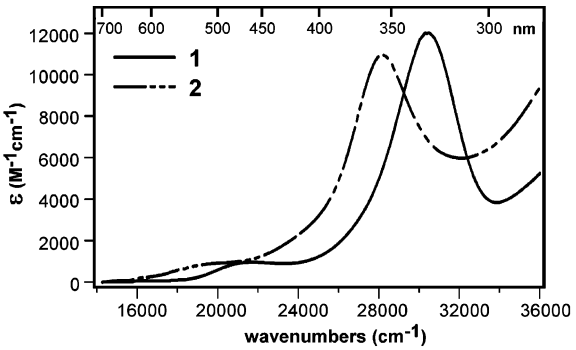

Figure 1. Room-temperature electronic absorption spectra of complexes **1** and **2** in MeCN solution.

Results and Analysis

1. Spectroscopic Results. A. Electronic Spectroscopy. The room temperature (RT) electronic absorption spectra of complexes **1** and **2** in MeCN are shown in Figure 1. The spectrum of complex **1** contains two prominent features: (i) a shoulder of weak intensity ($\epsilon \approx 1000$ M^{-1} cm^{-1}) centered at ~21 700 cm^{-1} and (ii) an intense band ($\epsilon = 12\,600$ M^{-1} cm^{-1}) in the near-UV region peaking at 30 400 cm^{-1}. While the overall appearance of the spectrum of **2** is quite similar, the corresponding weak and intense features are red-shifted to ~19 800 and 28 100 cm^{-1}, respectively. At energies greater than 32 000 cm^{-1}, both complexes exhibit a broad set of absorption bands that presumably arise from Fe(I) → CO(π*) charge transfer (CT) transitions. Although these spectra have been published previously,[26] their key features have remained largely unassigned.[44]

With the aim of resolving the bands that comprise the prominent spectroscopic features described above, electronic absorption and magnetic circular dichroism (MCD) spectra of **1** and **2** in frozen nitrile solutions were collected at 77 K. Compared to the RT spectra, the absorption bands observed in the low-temperature (LT) spectra are sharper and blue-shifted by nearly 500 cm^{-1} (Figure 2). As complexes **1** and **2** are diamagnetic, they do not display the temperature-dependent MCD signal intensity characteristic of ***C***-term behavior; instead, the MCD features seen in Figure 2 arise from temperature-independent ***B***-terms. For both complexes, simultaneous fitting of the LT absorption and MCD spectra requires three Gaussian bands (dotted lines in Figure 2) of roughly equal bandwidths along with an additional broad band to account for the intense near-UV features. Peak positions and intensities determined from these fits are listed in Table 1. For **1**, the dominant component within the low-

(30) (a) Baerends, E. J.; Ellis, D. E.; Ros, P. *Chem. Phys.* **1973**, *2*, 41. (b) Guerra, C. F.; Snijders, J. G.; te Velde, G.; Baerends, E. J. *Theor. Chem. Acc.* **1998**, *99*, 391−403. (c) te Velde, G.; Baerends, E. J. *J. Comput. Phys.* **1992**, *99*, 84−98. (d) Versluis, L.; Ziegler, T. *J. Chem. Phys.* **1988**, *88*, 322−328.
(31) Vosko, S. H.; Wilk, L.; Nusair, M. *Can. J. Phys.* **1980**, *58*, 1200−1211.
(32) Becke, A. D. *J. Chem. Phys.* **1986**, *84*, 4524−4529.
(33) Perdew, J. P. *Phys. Rev. B: Condens. Matter* **1986**, *33*, 8822−8824.
(34) Neese, F. *ORCA, Version 2.2.: An Ab Initio, Density Functional, and Semiempirical Program Package*; Max-Plack Institut für Bioanorganische Chemie: Mülheim an der Ruhr, Germany, 2001.
(35) Schaefer, A.; Horn, H.; Ahlrichs, R. *J. Chem. Phys.* **1992**, *97*, 2571.
(36) Ahlrichs, R. Unpublished results.
(37) (a) Eichkorn, K.; Treutler, O.; Ohm, H.; Haser, M.; Ahlrichs, R. *Chem. Phys. Lett.* **1995**, *240*, 283. (b) Eichkorn, K.; Weigend, F.; Treutler, O.; Ahlrichs, R. *Theor. Chem. Acc.* **1997**, *97*, 119.
(38) (a) Becke, A. D. *J. Chem. Phys.* **1993**, *98*, 5648−5652. (b) Becke, A. D. *J. Chem. Phys.* **1993**, *98*, 1372−1377.
(39) Lee, C. T.; Yang, W. T.; Parr, R. G. *Phys. Rev. B: Condens. Matter* **1988**, *37*, 785−789.
(40) (a) Bergman, D. L.; Laaksonen, L.; Laaksonen, A. *J. Mol. Graphics Modell.* **1997**, *15*, 301. (b) Laaksonen, L. *J. Mol. Graphics* **1992**, *10*, 33.
(41) (a) Stratmann, R. E.; Scuseria, G. E.; Frisch, M. J. *J. Chem. Phys.* **1998**, *109*, 8218−8224. (b) Casida, M. E.; Jamorski, C.; Casida, K. C.; Salahub, D. R. *J. Chem. Phys.* **1998**, *108*, 4439−4449. (c) Bauernschmitt, R.; Ahlrichs, R. *Chem. Phys. Lett.* **1996**, *256*, 454−464.
(42) (a) Hirata, S.; Head-Gordon, M. *Chem. Phys. Lett.* **1999**, *314*, 291−299. (b) Hirata, S.; Head-Gordon, M. *Chem. Phys. Lett.* **1999**, *302*, 375−382.
(43) Neese, F.; Olbrich, G. *Chem. Phys. Lett.* **2002**, *362*, 170−178.
(44) The following reference attributes the spectral features of the related complex $Fe_2(SCH_3)_2(CO)_6$ to transitions involving the Fe(I)−Fe(I) unit but does not provide specific transition assignments: Teo, B. K.; Hall, M. B.; Fenske, R. F.; Dahl, L. F. *Inorg. Chem.* **1975**, *14*, 3103−3117.

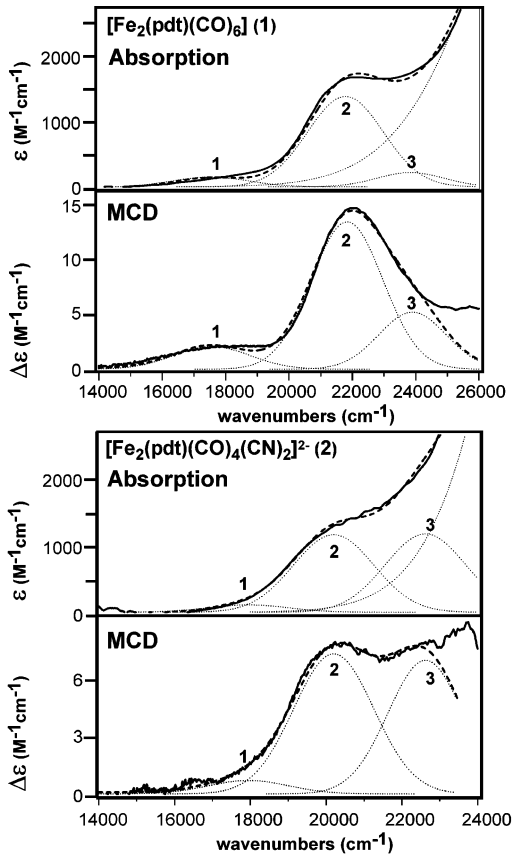

Figure 2. Gaussian-resolved (····) electronic absorption and MCD spectra of complexes **1** (top) and **2** (bottom). Spectra were obtained on frozen solutions in 1:1 propionitrile:butyronitrile mixtures (concentration = 2 mM) and collected with a magnetic field of 7 T at a temperature of 77 K. Band energies and parameters are summarized in Table 1. Note that the two sets of spectra are plotted over a different energy range; i.e., the *x* axes are not the same for **1** and **2**.

Table 1. Fit Parameters from Gaussian Deconvolutions of the Experimental Absorption and MCD Spectra of **1** and **2** (Figure 2)

band	ν_{max} (cm^{-1})	ϵ_{max} (M^{-1} cm^{-1})	osc str ($f_{exp} \times 10^3$)[a]	MCD intensity $\Delta\epsilon$ (M^{-1} cm^{-1})
		$Fe_2(pdt)(CO)_6$ (**1**)		
1	17 550	140	1.8	2.1
2	21 850	1380	18.0	13.4
3	23 900	220	2.5	5.2
		$[Fe_2(pdt)(CO)_4(CN)_2]^{2-}$ (**2**)		
1	17 950	90	1.0	0.8
2	20 200	1110	12.8	7.4
3	22 600	1130	13.0	7.0

[a] Oscillator strength, $f_{exp} = (4.61 \times 10^{-9})\epsilon_{max}\nu_{1/2}$.

energy absorption shoulder is band 2, while the other two bands carry only marginal intensity (ϵ < 300 M^{-1} cm^{-1}). For complex **2**, bands 2 and 3 possess comparable intensities in both the absorption and MCD spectra; however, the primary component of the low-energy shoulder is again band 2, as band 3 peaks at much higher energy.

1.B. Resonance Raman Spectroscopy. The solid-state resonance Raman (rR) spectrum of complex **1** obtained with 514 nm excitation (Figure 3a) exhibits two intense peaks at 205 and 356 cm^{-1} that are assigned to the Fe−Fe and totally symmetric Fe−S stretching modes, ν(Fe−Fe) and ν_s(Fe−S), respectively. These assignments are based on an earlier

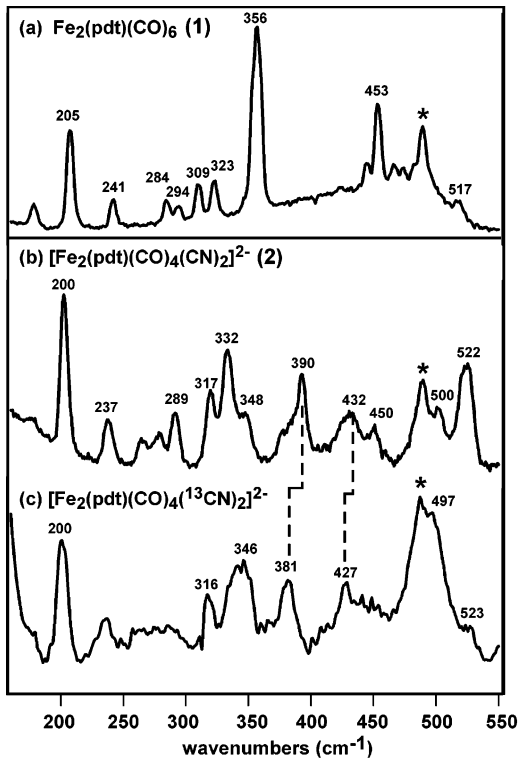

Figure 3. (a) 514.5 nm (19 436 cm^{-1}) excited rR spectrum of **1** in the solid state. (b) rR spectrum of **2** with natural abundance (NA) isotopes. (c) rR spectrum of **2** with ^{13}C-labeled cyano ligands. Both spectra of **2** were obtained using 568.2 nm (17 599 cm^{-1}) laser excitation. Peaks arising from the quartz sample holder are indicated by ∗.

Raman study performed by Scovell and Spiro on $Fe_2S_2(CO)_6$,[45] a complex that also possesses an Fe_2S_2 core with approximate C_{2v} symmetry. Most of the less intense features in the 280−330 cm^{-1} region arise from nontotally symmetric Fe−S stretching modes, while the peaks within the 440−520 cm^{-1} energy range are due to Fe−C(O) stretching and Fe−C−O bending modes, ν(Fe−C) and δ(Fe−C−O), respectively. These assignments were further corroborated by DFT frequency calculations performed on a geometry-optimized model of **1** (Table S1).[46] In the high-energy region, multiple bands that can be ascribed to modes primarily involving C═O stretching motions are observed between 1900 and 2050 cm^{-1}; however, as these features are not resonance enhanced, they possess little intensity (data not shown). rR spectra obtained for frozen MeCN solutions of **1** (Figure S1a) are similar to the solid-state data, displaying only minor shifts in peak positions (<3 cm^{-1}).

By comparison to **1**, the rR spectrum of the dicyano-substituted complex **2** (Figure 3b) is more complex because of the lower symmetry of this dimer in the solid state (C_1 symmetry for **2**[16] as opposed to approximate C_{2v} symmetry for **1**). The two cyano ligands occupy one axial (trans to the

(45) Scovell, W. M.; Spiro, T. G. *Inorg. Chem.* **1974**, *13*, 304−308.
(46) In excellent agreement with our experimental rR data, the DFT-calculated frequencies for the ν(Fe−Fe) and ν_s(Fe−S) modes are 194 and 340 cm^{-1}, respectively, and those for the nontotally symmetric ν(Fe−S) modes are 269 (a_2), 290 (b_1), and 300 (b_2) cm^{-1} (Table S1). The computed frequencies for the ν(Fe−C) and δ(Fe−C−O/N) modes fall within the range of 400−600 cm^{-1}. See Supporting Information for more details.

Fe−Fe bond vector) and one basal (trans to one Fe−S bond) position (Scheme 2). Thus, the two thiolate sulfurs are inequivalent, resulting in the appearance of two features at 348 and 332 cm^{-1} that mainly involve symmetric Fe−S−Fe stretching motions rather than a single intense peak as observed for **1**. The two antisymmetric Fe−S−Fe stretching modes likely contribute to the series of peaks between 250 and 320 cm^{-1}, and the intense peak at 200 cm^{-1} is readily attributed to the ν(Fe−Fe) mode.[45] In frozen MeCN solutions of **2**, the two cyano ligands sample multiple fixed orientations with respect to the Fe−Fe bond, causing the 348 and 332 cm^{-1} peaks observed in the solid state to collapse into a single broad feature centered at 342 cm^{-1} (Figure S1b).

For **2**, the ν(Fe−C) and δ(FeCO)/δ(FeCN) modes span a wide energy range from 380 to 525 cm^{-1}. To unambiguously assign these bands to vibrations involving either the carbonyl or cyano ligands, complex **2** was also synthesized using ^{13}C-labeled cyanide; the corresponding rR spectrum is displayed in Figure 3c. Upon isotopic substitution, the 390 and 432 cm^{-1} peaks in the natural abundance (NA) spectrum of **2** downshift by 9 and 5 cm^{-1}, respectively. The energies of two additional features, at 450 and 500 cm^{-1}, also appear to be altered by ^{13}CN-substitution, but it is difficult to discern the magnitude of their energy shifts. IR data gathered in MeCN solution reveal that the ν(C−N) mode at 2075 cm^{-1} in the spectrum of the NA dimer shifts to 2029 cm^{-1} upon isotopic substitution (data not shown). This 46 cm^{-1} downshift is close to the 43 cm^{-1} shift predicted for a simple harmonic oscillator. Upon $^{12}C \rightarrow {}^{13}C$ isotopic substitution, the energies of the Fe−S stretching modes remain unchanged to within the experimental error of ± 1 cm^{-1}; however, sizable changes in the relative intensities of these modes are apparent. This result suggests that the vibrations of the Fe_2S_2 core are coupled to those of the FeC(O/N) units, a result that is confirmed by our normal-coordinate analysis for complex **2** (vide infra).

1.C. Resonance Raman Excitation Profiles. Figure 4 shows the rR excitation profiles of the 205 and 356 cm^{-1} modes of complex **1** superimposed on the corresponding LT absorption spectrum along with band 2 (dotted line) as resolved by the spectral deconvolution. The rR profiles in Figure 4 were collected on a dilute, frozen solution of **1** in MeCN using the solvent peak at 390 cm^{-1} as the internal intensity standard. While the overall shapes of the profiles associated with the 356 and 205 cm^{-1} modes are similar, the former has approximately twice the intensity of the latter over the full range of excitation energies. Attempts to measure rR data at higher energies (>24 000 cm^{-1}) were unsuccessful because of significant sample decomposition. Nearly identical profiles were obtained with solid-state samples (data not shown).

Interestingly, the excitation profiles shown in Figure 4 do not follow the usual relationship between absorption and rR intensities, as typically the maxima of the absorption envelope and rR profile roughly coincide. Instead, while the expected preresonance enhancement is observed for excitation energies less than ~20 000 cm^{-1}, the 205 and 356 cm^{-1} modes exhibit large *decreases* in intensity as the laser

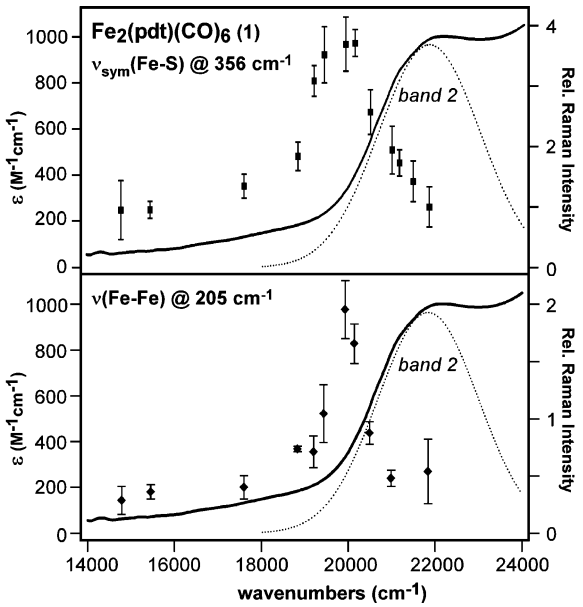

Figure 4. rR excitation profiles of the 356 cm^{-1} (top) and 205 cm^{-1} (bottom) modes of **1** measured on frozen MeCN solutions (concentration ≈ 5 mM) at 77 K. The error bars represent the standard deviation of rR intensities obtained from at least three independent data sets. Profiles are superimposed on the corresponding 77 K absorption spectrum. Band 2 from the Gaussian deconvolutions in Figure 2 is shown for comparison (dotted line).

excitation approaches the low-energy shoulder, reaching apparent minima near the greatest intensity of band 2. This unusual behavior is not due to reabsorption of the scattered photons as the solutions studied were quite dilute (~5 mM) and the 390 cm^{-1} reference (solvent) peak is close in energy to the peaks under study. Nor is the profile shape affected by sample decomposition, since these data were obtained using short exposure times with low laser power (see Experimental Section), and the samples were found to degrade quite slowly even with 458 nm excitation. Instead, this apparent resonance de-enhancement evident in Figure 4 is due to a well-established phenomenon that has been observed for several transition-metal systems. Zink and coworkers have demonstrated that rR de-enhancement results from interference between the excited electronic state of interest and other nearby excited states.[47] In this case, the interfering excited state(s) correspond to the intense absorption feature in the near-UV (vide infra).

For comparison, the rR excitation profile of the ν(Fe−S) mode of complex **2** observed at 342 cm^{-1} in the frozen MeCN solution spectrum (Figure 5) was obtained using similar experimental methods.[48] This profile also exhibits sizable resonance de-enhancement, although the decline in rR intensity is less dramatic than that observed for the profiles of **1** (I_{max}/I_{min} = 3.9 (average) for **1** and 2.7 for **2**). Significantly, since the absorption features of **2** are red-shifted by ~2000 cm^{-1} compared with those of **1**, it was

(47) (a) Bailey, S. E.; Cohan, J. S.; Zink, J. I. *J. Phys. Chem. B* **2000**, *104*, 10743−10749. (b) Shin, K. S. K.; Zink, J. I. *J. Am. Chem. Soc.* **1990**, *112*, 7148−7157.

(48) In solution, the 200 cm^{-1} mode of **2** is substantially broadened and often appears on the slope associated with the Rayleigh scattering peak. Therefore, it was not possible to obtain a high-quality rR profile for this mode.

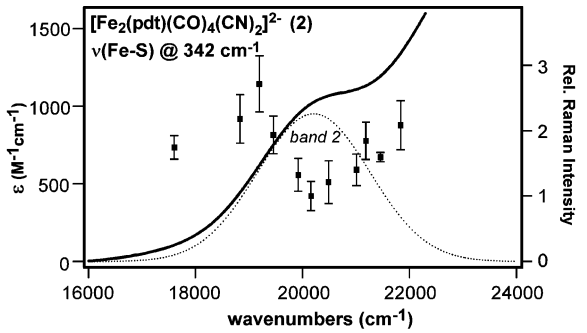

Figure 5. rR excitation profile of the 342 cm^{-1} mode of **2** measured on frozen MeCN solutions (concentration ≈ 5 mM) at 77 K. The profile is superimposed on the corresponding 77 K absorption spectrum. Band 2 from the Gaussian deconvolutions in Figure 2 is shown for comparison (dotted line).

possible to collect data over the entire span of the low-energy shoulder. The resulting profile exhibits a well-defined intensity minimum at ~20 200 cm^{-1} (496 nm excitation) near the maximum of band 2. At higher excitation energies, the mode intensity is seen to increase again due to preresonance scattering associated with features in the near-UV region.

2. Normal-Coordinate Analysis (NCA). The normal-coordinate analyses described herein utilized a general valence force field. For complex **1**, the large size of the molecule forced us to use a smaller model in our NCA treatment, in which the following simplifications were made: (i) the $-C_3H_6-$ linkage in the pdt ligand was eliminated, (ii) the CO ligands were treated as single atoms with an effective mass of 28 amu, and (iii) the X-ray structure coordinates were symmetrized to obtain a molecule with strict C_{2v} symmetry. Furthermore, although the axial and basal carbonyl ligands are not symmetry equivalent, only one force constant was used to describe both sets of Fe−C(O) stretching motions.

In generating the molecular force field of complex **1**, initial guesses for several force constants were based on the rR study of $Fe_2S_2(CO)_6$ performed by Scovell and Spiro.[45] A small S···S force constant of +0.20 mdyn/Å was included to model the nonbonded interaction between the two bridging sulfur atoms. The optimized set of force constants for **1** is shown in Table 2. Not surprisingly, the force constants for **1** and the previously characterized dimer $Fe_2S_2(CO)_6$ are quite similar, although those associated with stretching motions are smaller by 0.10−0.15 mdyn/Å in the former complex.[45] To reproduce the frequencies of the nontotally symmetric ν_{as}(Fe−S) modes, it was necessary to include nonzero interaction force constants, accounting for kinematic coupling between the stretching motions of adjacent Fe−S bonds. As revealed by the calculated frequencies and the potential energy distributions (PEDs) of modes primarily involving nuclear motions of the Fe_2S_2 core (Table 3), our NCA yields frequencies for the ν(Fe−Fe) and symmetric ν_s(Fe−S) modes that are identical to the experimental values. Additionally, the calculated frequencies of 274, 289, and 328 cm^{-1} for the three asymmetric ν_{as}(Fe−S) modes agree well with the 280−330 cm^{-1} energy range provided experimentally, and the calculated energies of the six ν(Fe−C) modes all lie within the experimental range of 440−520 cm^{-1}. The PEDs

Table 2. Force Constants Obtained from the Normal-Coordinate Analyses for **1** and **2**

$Fe_2(pdt)(CO)_6$ **(1)**			
Stretching (mdyn/Å)			
Fe−Fe	1.20	S···S	0.20
Fe−S	1.50	Fe−C(O)	2.35
Bending (mdyn·Å/rad^2)			
C−Fe−C	0.10		
Interaction (mdyn/Å)			
Fe−S/Fe−S[a]	0.05	Fe−S/Fe−S[b]	−0.15
$[Fe_2(pdt)(CO)_4(CN)_2]^{2-}$ **(2)**			
Stretching (mdyn/Å)			
Fe−Fe	1.12	Fe−C(O)	2.58
Fe−S	1.33	Fe−C(N)	1.83
S···S	0.20	C−N	16.16
Bending (mdyn·Å/rad^2)			
C−Fe−C	0.10	Fe−C−N	0.45
Interaction[c]			
Fe−C(N)/C−N[d]	0.30	Fe−C(N)/Fe−C−N[e]	0.10

[a] Interaction between Fe−S stretching motions for which Fe is the common atom. [b] Same as (a), but with S as the common atom. [c] Interaction constants between Fe−S stretching modes were not included in the NCA of **2** (see ref 50). [d] Interaction constant between Fe−C(N) and C−N stretching motions, in mdyn/Å. [e] Interaction constant between Fe−C(N) stretching and Fe−C−N bending motions, in mdyn/rad.

for the ν(Fe−S) modes shown in Table 3 reveal a significant degree of mechanical coupling between the Fe−S and Fe−C stretching motions. In particular, the totally symmetric ν_s-(Fe−S) mode contains substantial (25%) contributions from the Fe−C stretching motions of the basal carbonyl ligands, which is a result of the trans orientation of thiolate and basal CO ligands.

The NCA of complex **2** presented additional complications due to the mixed CO/CN ligation and the lower molecular symmetry (C_1 in the solid state). Consequently, the NCA of **2** required many of the same assumptions and simplifications used to treat complex **1**.[49] For instance, despite the C_1 symmetry of **2**, all Fe−S stretches were assigned the same force constant, and a single value was used for the C−Fe−C bending motions regardless of the identities of the diatomic ligands (CO or CN).[50] To calculate the isotope shifts in the rR spectrum of the ^{13}CN-labeled complex, it was necessary to treat the cyano ligands as true diatomics by including the C−N stretching and Fe−C−N bending motions. In accordance with previous vibrational studies of FeCN units in synthetic complexes and heme systems,[51] the force field

(49) The following approximations were also made for **2**: (i) the elimination of the propane linkage in the pdt ligand, (ii) the modeling of CO ligands as single atoms, (iii) the inclusion of a small S···S interaction force constant, and (iv) the use of a single force constant for inequivalent internal coordinates involving the same set of atoms.

(50) Because of the symmetry inequivalence of all four Fe−S bonds in **2**, the corresponding force constants are expected to show some variation. Consequently, when carrying out a NCA for **2**, it is impossible to separate the role of interaction force constants from the differences in Fe−S force constants on the calculated frequencies of the ν(Fe−S) modes. As reasonable frequencies for these modes were calculated using a single set of Fe−S force constants and without inclusion of interaction force constants, these approximations should have only minor impact on the quality of the final force field. Nevertheless, the Fe−S stretching force constants determined for **2** are subject to somewhat greater uncertainties than those obtained for **1**.

Table 3. Comparison of Experimental and Calculated Vibrational Data for **1**

mode	sym[a]	NCA ν (cm^{-1})	Exp ν (cm^{-1})	potential energy distributions, PED (%)				
				Δr(Fe−Fe)	Δr(Fe−S)	Δr(S−S)	Δr(Fe−CO_{ax})	Δr(Fe−CO_{bas})
ν(Fe−Fe)	a_1	205	205	74	3	8	10	1
ν_{as}(Fe−S)	a_2	274	280−330	0	85	0	0	14
ν_{as}(Fe−S)	b_1	289		0	80	0	3	16
ν_{as}(Fe−S)	b_2	328		0	81	0	0	19
ν_{s}(Fe−S)	a_1	356	356	0	59	9	8	25

[a] Symmetry labels are given assuming effective C_{2v} symmetry.

Table 4. Comparison of Experimental and Calculated Vibrational Data for **2**

mode	NCA		exp		potential energy distributions, PED (%)					
	ν(cm^{-1})	Δ(^{13}CN)[a]	ν(cm^{-1})	Δ(^{13}CN)[a]	Δr(Fe−Fe)	Δr(Fe−S)	Δr(S−S)	Δr(Fe−C(O))	Δr(Fe−C(N))	$\Delta\alpha$(FeCN)[c]
ν(Fe−Fe)	200		200		74	3	9	5	6	0
ν(Fe−S)	330		332		0	76	0	10	12	1
ν(Fe−S)	351		348		0	58	7	19	14	1
δ(Fe−C−N)	391	10	390	9	0	8	0	3	12	76
ν(Fe−C(N))$_{ax}$	429	4	432	5	4	5	0	3	81	4
ν(Fe−C(N))$_{bas}$	454	4	450		1	16	0	15	59	7
ν(C−N)[b]	2074	45	2075	46						

[a] Isotopic shifts for ^{12}CN → ^{13}CN substitution. [b] The PED of the ν(C−N) mode is not provided, as this mode is ∼95% C−N stretching in character. [c] Movement along Fe−C−N bending motion.

employed interaction force constants between the Fe−C(N) and C−N stretching motions and between the Fe−C(N) stretching and Fe−C−N bending motions. The values used for these off-diagonal terms were taken from published NCA results obtained for analogous FeCN systems[51] and were not adjusted to fit the experimental data. With the parameters calculated above for complex **1** as initial guesses for the remaining force constants, a force field was generated for **2** that accurately predicts the vibrational frequencies and isotope shifts of key normal modes (Table 4). As shown in Table 2, the force constants for the Fe−Fe and Fe−S stretches are somewhat reduced compared to those calculated for **1**, while the corresponding Fe−C(O) force constant increases by 0.23 mdyn/Å upon dicyano substitution. On the basis of the magnitude of their shifts, the two isotopically active modes at 390 and 430 cm^{-1} are assigned to δ(Fe−C−N) and axial ν(Fe−C(N)) modes, respectively. Moreover, the NCA predicts a frequency of 454 cm^{-1} for the basal ν(Fe−C(N)) mode, permitting assignment of the additional isotopically sensitive feature at 450 cm^{-1} in the experimental rR spectrum (Figure 3b) to this mode.[52]

While vibrational studies of Fe(I) systems with carbonyl and cyano ligands are quite rare, it is interesting to compare the NCA results described above to those obtained with Fe−C(O/N) species in other metal oxidation states. A survey of the literature, combined with the results from this study, suggests that Fe−C(O) stretching force constants in five- and six-coordinate systems remain relatively constant as the oxidation state is lowered from Fe(II) → Fe(I) → Fe(0), typically falling in the range of 2.30−2.65 mdyn/Å.[53,54] This result suggests that the two major contributions to Fe−CO bonding, σ donation and π-backbonding, are similarly balanced in these systems. As the Fe center becomes more electron rich upon reduction, its ability to engage in Fe−CO π-backbonding interactions increases, which will significantly strengthen Fe−CO bonds.[55] But for oxidation states lower than Fe(II), the transferred electron enters the Fe(e_g) set of d orbitals, which are σ antibonding with respect to the Fe−C bonds. Moreover, σ donation decreases due to the increased energy splitting between the CO lone pairs and the Fe(e_g) orbitals. Collectively, these multiple and competing effects result in Fe−C stretching force constants in Fe−carbonyl systems that are largely invariant to changes in metal oxidation state.

Alternatively, for Fe−cyano complexes, reduction from Fe(III) to Fe(II) increases the Fe−C stretching constant from ∼ 1.7 to 2.4 mdyn/Å[51] because the added electron enters the Fe(t_{2g}) set of orbitals that directly participate in Fe−CN π-backbonding interactions. Our NCA of complex **2**, though,

(51) (a) Kim, Y.; Babcock, G. T.; Surerus, K. K.; Fee, J. A.; Dyer, R. B.; Woodruff, W. H.; Oertling, W. A. *Biospectroscopy* **1998**, *4*, 1−15. (b) Lopez-Garriga, J. J.; Oertling, W. A.; Kean, R. T.; Hoogland, H.; Wever, R.; Babcock, G. T. *Biochemistry* **1990**, *29*, 9387−9395. (c) Nakagawa, I.; Shimanouchi, T. *Spectrochim. Acta* **1962**, *18*, 101−113.

(52) As the same Fe−C−N and C−N force constants were used for both CN ligands and the δ(Fe−C−N) and ν(C−N) modes are largely uncoupled to the motions of the Fe−S core, the calculated frequencies for these two modes are nearly identical for the axial and basal CN ligands. Conversely, the axial and basal ν(Fe−CN) modes have distinct frequencies due to different degrees of vibrational coupling with the Fe−S stretching motions (Table 4).

(53) (a) Li, X. Y.; Spiro, T. G. *J. Am. Chem. Soc.* **1988**, *110*, 6024−6033. (b) Yu, N. T.; Benko, B.; Kerr, E. A.; Gersonde, K. *Proc. Natl. Acad. Sci. U.S.A.* **1984**, *81*, 5106−5110. (c) Jones, L. H.; Goldblat, M.; Swanson, B. I.; McDowell, R. S. *J. Chem. Phys.* **1972**, *57*, 2050−2064 and references therein.

(54) The exception to this statement is the complex $[Fe(II)(CO)_6]^{2+}$, for which an Fe−C force constant of 1.673 mdyn/Å was determined. It appears that the large positive charge of this complex, which is distributed over a relatively small number of atoms, significantly reduces the strength of the Fe−CO π-backbonding interaction, leading to weaker Fe−C bonds. See the following reference: Bernhardt, E.; Bley, B.; Wartchow, R.; Willner, H.; Bill, E.; Kuhn, P.; Sham, I. H. T.; Bodenbinder, M.; Bröchler, R.; Aubke, F. *J. Am. Chem. Soc.* **1999**, *121*, 7188−7200.

(55) (a) Loschen, C.; Frenking, G. *Inorg. Chem.* **2004**, *43*, 778−784. (b) Dietz, O.; Rayon, V. M.; Frenking, G. *Inorg. Chem.* **2003**, *42*, 4977−4984. (c) Ehlers, A. W.; Dapprich, S.; Vyboishchikov, S. F.; Frenking, G. *Organometallics* **1996**, *15*, 105−117.

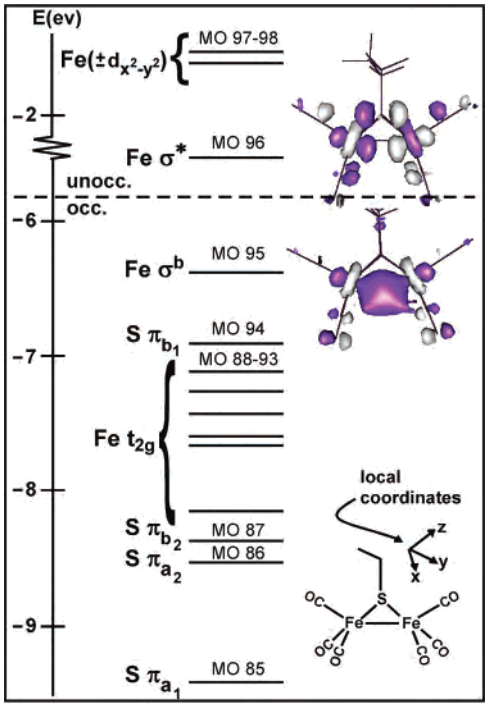

Figure 6. MO energy diagram for **1** obtained from a spin-restricted DFT calculation. MOs are labeled according to their principal contributors. MO isosurface plots for the HOMO (no. 95) and LUMO (no. 96) are shown in the upper right.

suggests that Fe−C(N) bond strength is significantly diminished in Fe(I) systems compared to that of Fe(II) systems (1.8 mdyn/Å for **2**, ~2.4 mdyn/Å for Fe(II)), indicating that the electronic effects described above are no longer balanced. A rationale for these observations lies in previous studies that have shown that the Fe−C(N) bond strength is primarily derived from σ interactions not π interactions.[55] This is a result of the negative charge of the CN ligand, which greatly destabilizes the π^* orbitals of CN relative to those of CO. Consequently, the addition of an electron to an $e_g(\sigma^*)$ orbital upon reduction from Fe(II) → Fe(I) only serves to weaken the Fe−C(N) σ bond without significantly strengthening the Fe−C(N) π bond.

3. Computational Results. A. DFT Bonding Description. To develop quantitative bonding descriptions for complexes **1** and **2**, restricted density functional theory (DFT) calculations were performed using the B3LYP hybrid functional. The input geometries for these single-point calculations were based directly on the corresponding X-ray crystal structures.[16,17] The resulting bonding scheme for complex **1**, as shown in Figure 6, largely conforms to the molecular orbital (MO) scheme developed previously for $Fe_2(SR)_2(CO)_6$-type complexes.[44,56] Ignoring the direct Fe−Fe interaction, each Fe center exists in a distorted square-pyramidal ligand environment with the local *z* axis directed toward the axial CO ligand, and the two low-spin Fe(I) centers each possess $(t_{2g})^6(e_g)^1$ configurations in which the lone e_g-based electron resides in the d_{z^2}-based MO. However, in the dimer structure, the 10 Fe d orbitals combine to form symmetry-adapted MOs that are either bonding or antibonding with respect to the Fe−Fe bond vector. The highest occupied MO (HOMO) of **1**, MO 95, corresponds to the bonding combination of the Fe(I) d_{z^2} orbitals (Figure 6); it is labeled σ^b using the standard nomenclature of metal−metal bonding. This MO, which is the source of the "bent" Fe−Fe single bond,[56] is characterized by a large lobe of electron density below the internuclear axis, making the complex reactive toward electrophiles such as H^+.[19] The lowest unoccupied MO (LUMO) of **1** is the antibonding combination of the Fe(I) d_{z^2} orbitals, labeled σ^* in Figure 6 (MO 96). At higher energy lie the unoccupied symmetric and antisymmetric linear combinations of the Fe(I) $d_{x^2-y^2}$ orbitals. In agreement with earlier photoelectron spectroscopic (PES) studies,[23] complex **1** generally follows the "normal bonding scheme" in which the Fe(I) d-based MOs lie higher in energy than the S-based MOs, although MO 94 is largely sulfur-based. MOs 88−93 arise from the bonding and antibonding combinations of the six Fe(I) t_{2g} orbitals but also contain significant contributions from the S 3p orbitals and, to a lesser extent, the CO π^* orbitals (Table S2).

Complex **2**, which is isoelectronic with **1**, follows the same overall bonding scheme in which the HOMO and LUMO are the Fe(I)-based σ^b and σ^* MOs, respectively. Yet important differences between these two complexes are revealed by their respective orbital compositions. The substitution of two neutral carbonyl ligands by anionic cyanide moieties raises the relative energies of the Fe d orbitals, increasing their energetic separation from the S 3p orbitals while diminishing their separation from the unoccupied CO π^* orbitals. These changes are reflected in the relative compositions of the Fe(I) d-based MOs. The percentage of sulfur contribution to MOs 88−98 decreases from an average of 18.1% for **1** to 15.8% for **2** (Tables S2 and S3). Conversely, the average contribution of the six diatomic ligands (CO/CN) to these MOs increases from 20.1% in **1** to 27.5% in **2**. Both trends are even more pronounced for MOs near the HOMO/LUMO gap. Thus, the net effect of cyanide substitution is to reduce Fe−S bond covalency while strengthening the remaining Fe−CO bonds through enhanced π-backbonding interactions. These results also provide a rationale for the observation, made by Rauchfuss and coworkers, that no more than two CO ligands of **1** can be substituted by CNs even in the presence of a large excess of CN.[16] Our DFT results indicate that carbonyl → cyanide substitution at the Fe(I) centers increases the strength of the remaining Fe−CO bonds, thus hindering further ligand substitution on the dimer (note that electrostatic factors will likely enhance this effect, as CN substitution results in a negative charge build up on the cluster). Importantly, these computational insights are nicely corroborated by our analysis of the rR data presented above, which indicates that dicyano substitution weakens the Fe−S bonds while strengthening the remaining Fe−CO bonds (see the experimentally derived force constants in Table 2).

3.B. Time-Dependent DFT Results: Spectral Assignments As a further test of our computational methodology,

(56) (a) Anderson, E. L.; Fehlner, T. P.; Foti, A. E.; Salahub, D. R. *J. Am. Chem. Soc.* **1980**, *102*, 7422−7429. (b) DeKock, R. L.; Baerends, E. J.; Hengelmolen, R. *Organometallics* **1984**, *3*, 289−292.

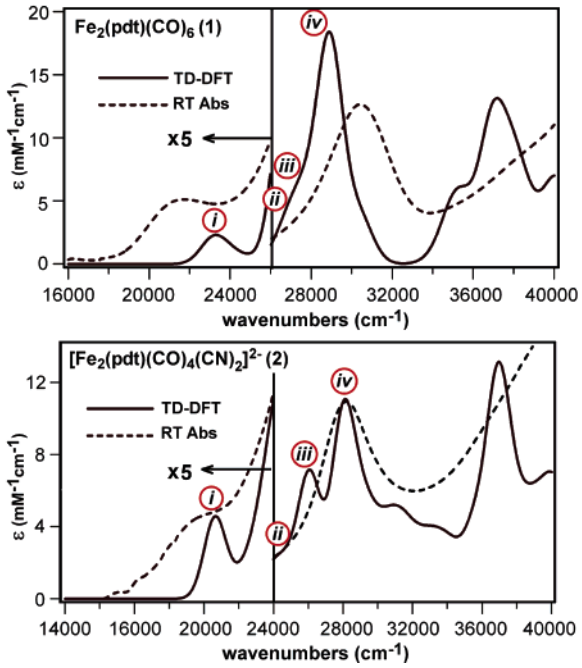

Figure 7. TD-DFT computed absorption spectra (solid lines) for complex **1** (top) and complex **2** (bottom). The experimental RT absorption spectra are also shown for comparison (dashed lines). Transitions producing the dominant contributions to the computed spectra are labeled *i*−*iv* (see Figure 8). Note that the two sets of spectra are plotted over a different energy range; i.e., the *x* axes are not the same for **1** and **2**.

absorption spectra of complexes **1** and **2** were calculated using the B3LYP hybrid functional and the TD-DFT method within the Tamm−Dancoff approximation (TDA).[41,42] In each case, the TD-DFT calculations were performed using the full molecular structure as determined by X-ray crystallography, omitting only the counterions. The computed spectra for **1** and **2** are displayed in Figure 7, along with the experimental RT absorption spectra. For both complexes, the calculated spectra reproduce the two primary features observed experimentally remarkably well, namely, the weak shoulder in the visible region and the intense band in the near-UV region. The calculations also properly predict multiple transitions above 32 000 cm^{-1} and reveal that these transitions primarily involve Fe(I) 3d → CO π^* CT excitations. Further, in excellent agreement with the spectral deconvolutions of the absorption and MCD data presented above (Figure 2), the calculated low-energy absorption features are each composed of three components, two weak and one strong. For complex **1**, the predicted band energies and intensities agree reasonably well with the experimental data, although the calculation slightly underestimates the energy of the intense UV band by ∼1400 cm^{-1} and overestimates the energy of the low-energy shoulder by about the same amount. For complex **2**, the agreement between the experimental and calculated spectra is even better in terms of both energies and intensities.

The TD-DFT method also provides information regarding the donor and acceptor orbitals for each calculated transition, permitting unambiguous assignments of the key spectral features. Specifically, for complex **1**, our computations indicate that the dominant contributor to the intense UV absorption band primarily involves HOMO → LUMO [Fe(σ^b) → Fe(σ^*)] excitation (transition *iv*, Figure 8). The most intense transition contributing to the weak, low-energy shoulder (transition *i*) is assigned as the HOMO-2 → LUMO excitation (no. 93 → no. 96), and transitions *ii* and *iii* also involve promotion of an electron from Fe(I) t_{2g}-based MOs to the LUMO (Figure 8). Thus, all absorption features below 32 000 cm^{-1} arise from transitions within the Fe(I)−Fe(I) core. On the basis of the MO diagram in Figure 8, it is perhaps perplexing that transitions *i*−*iii* are computed lower in energy than transition *iv*; however, it is crucial to

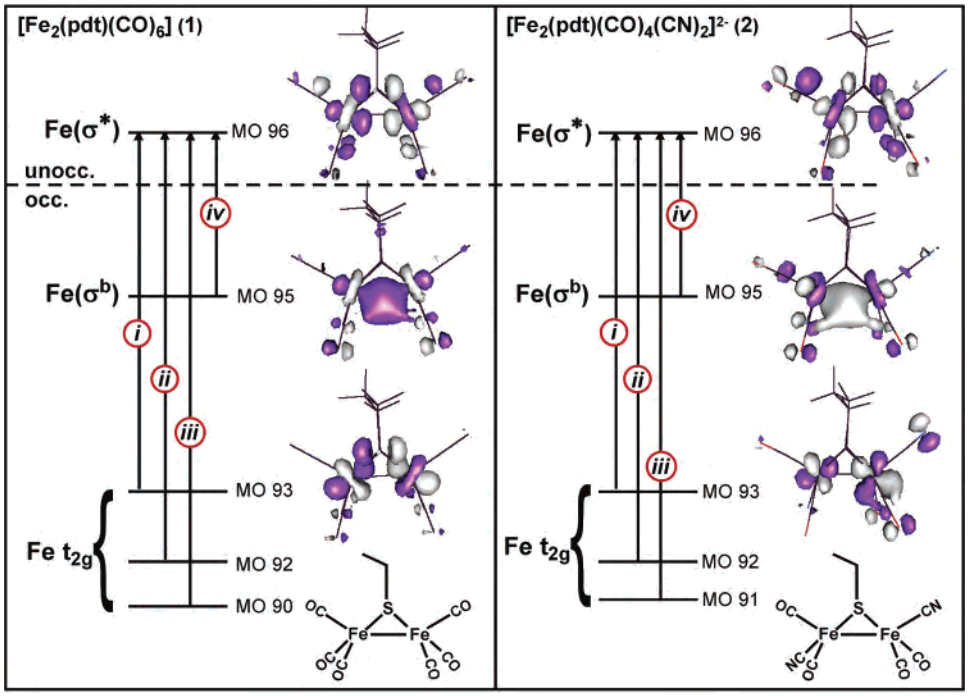

Figure 8. Isosurface plots of the key MOs involved in the electronic transitions *i*−*iv* of the TD-DFT computed absorption spectra of **1** (left) and **2** (right).

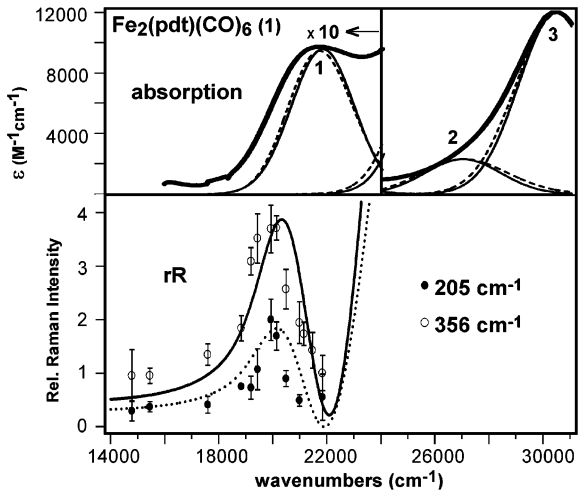

Figure 9. Experimental and simulated absorption and rR excitation profile data for complex **1**. Top: Experimental RT absorption spectrum (thick solid line) and Gaussian-resolved bands 1−3 (thin solid lines) along with simulated band shapes (dashed lines). Bottom: Experimental rR excitation profiles (symbols) and the corresponding simulations (solid and dotted lines for 356 and 205 cm^{-1} modes, respectively). All simulated data were obtained using time-dependent Heller theory along with the parameter set listed in Table 5.

remember that electronic relaxation in the excited state greatly affects the actual transition energy.

As shown in Figure 8b, the TD-DFT results for complex **2** reveal that transitions *i*−*iv* are similar in nature to their counterparts of **1**. On the basis of these results, the dominant band at 28 100 cm^{-1} in the experimental spectrum of **2** is attributed to the Fe(σ^b) → Fe(σ^*) transition, and the features to lower energy are assigned to Fe(t_{2g}) → Fe(σ^*) transitions. One important difference between **1** and **2**, though, relates to the reduction in Fe−S covalency upon dicyano substitution, which alters the composition of the MOs involved in transition *i*. While in complex **1**, the donor MO of transition *i* (MO 93) contains a substantial amount (15%) of sulfur orbital character, the corresponding MO of **2** lacks such a contribution, although thiolate character remains in the LUMO of both complexes (Figure 8, Tables S2 and S3). Thus, it would be expected that transition *i* results in smaller Fe−S bond distortions in **2** than in **1**. This prediction is nicely verified by our analysis of the rR excitation profiles presented in the next section.

4. Simulation of rR Excitation Profiles. To gain insights into the excited-state distortions experienced by **1** and **2**, a quantitative analysis of the rR excitation profile data was performed using the time-dependent theory of Heller.[28,29] As noted above, the resonance de-enhancement observed in the rR excitation profiles is the result of destructive interference between the Raman scattering cross-sections associated with multiple excited states.[47] Thus, simulation of the profile data required the extraction of certain excited-state parameters from the experimental absorption spectra, namely, the zero−zero transition energies (E_{00}) and relative intensities of the bands associated with the interacting excited states. For complex **1**, simultaneous fitting of the absorption spectrum and rR profiles required the use of a three-state model (Figure 9, top). With reference to the spectral analysis presented in the previous section, the first and third excited states correspond to transitions *i* and *iv*, respectively, while the second excited state is used to account for the collective presence of transitions *ii* and *iii* (thereby limiting the number of parameters used in our analysis).

Table 5. Excited State Parameters Determined by Simultaneous Fitting of the Absorption and rR Excitation Profile Data of **1** and **2**

parameters[a]	state 1	state 2	state 3
	(a) $Fe_2(pdt)(CO)_6$ (**1**)		
E_{00} (cm^{-1})	18 600	21 500	24 950
Δ_{205}	3.5	5.5	5.5
Δ_{356}	3.3	3.8	3.8
μ^2_{rel}	1	2.5	15
	(b) $[Fe_2(pdt)(CO)_4(CN)_2]^{2-}$ (**2**)		
E_{00} (cm^{-1})	17 550	20 300	23 700
Δ_{200}	3.2	5.0	5.0
Δ_{342}	2.2	2.4	2.4
μ^2_{rel}	1	2	10

[a] E_{00} is the energy of the zero−zero transition, Δ_k is the displacement along the *k*th mode, and μ^2_{rel} is the relative square of the transition dipole moment (where μ^2 is proportional to the experimentally determined oscillator strength).

In Heller theory, the distortion of an excited state, *n*, along a given normal mode, *k*, is expressed by the dimensionless parameter, $\Delta_{k,n}$. The relative distortions along two modes, *k* and *k*′, can be estimated using the Savin formula:[57]

$$\frac{I_k}{I_{k'}} = \left(\frac{\Delta_k \omega_k}{\Delta_{k'} \omega_{k'}}\right)^2 \quad (1)$$

where I_k ($I_{k'}$) and ω_k ($\omega_{k'}$) are the corresponding rR intensity and vibrational frequency, respectively. Using eq 1 along with the rR data in Figure 3, an initial Δ_{205}:Δ_{356} ratio of 5:4 was obtained. From this starting point, the $\Delta_{205,n}$ and $\Delta_{356,n}$ parameters in the three excited states (n = 1, 2, 3) were systematically varied to yield the best fits of the rR profiles although, for the sake of simplicity, the second and third excited states were assumed to have the same Δ values ($\Delta_{k,2} \equiv \Delta_{k,3}$). The best-fit parameters obtained in solving this two-mode/three-state problem are summarized in Table 5.[58] As expected, the shapes of the calculated profiles are most sensitive to distortions in the first excited state; however, due to the very nature of the interference mechanism responsible for the de-enhancement phenomenon, the Δ values associated with the two higher-energy excited states also exert considerable influence over the quality of the fits. Interestingly, accurate fits of the experimental data require that distortions along both modes are larger in the higher-energy excited states than in the first excited state ($\Delta_{k,1} < \Delta_{k,2} \equiv \Delta_{k,3}$), a requirement that is particularly stringent for the Δ_{205} parameter (Table 5). Figure 9 illustrates that with the set of parameters in Table 5, a satisfactory correspondence is achieved between both the experimental and simulated rR profiles, and the energies and widths of the

(57) (a) Savin, F. A. *Opt. Spektrosk.* **1965**, *19*, 555. (b) Warshel, A.; Dauber, P. *J. Chem. Phys.* **1977**, *66*, 5477. (c) Heller, E. J.; Sundberg, R. L.; Tannor, D. L. *J. Phys. Chem.* **1982**, *86*, 1822.

(58) Given the experimental uncertainties inherent to both the rR profiles and the excited-state parameters extracted from the absorption spectra, the values determined for **1** are estimated to be accurate within ±0.2 units.

principal absorption features are also well reproduced by the Heller analysis. Most notably, the calculated rR profiles nicely account for the strong resonance de-enhancement observed experimentally.

The rR profile of the 342 cm^{-1} mode of complex **2** was also analyzed in terms of a two-mode/three-state problem, even though we were unable to obtain an experimental rR profile of the corresponding ν(Fe−Fe) normal mode. To overcome this deficiency, the Δ parameters for this mode were assumed to be similar to those determined for **1**. Given the need for this assumption, the resulting set of Δ parameters listed in Table 5 should be considered as being subject to somewhat greater experimental uncertainties (a comparison between experimental and simulated spectroscopic data for **2** is provided in Figure S2). Despite this limitation, it is quite clear that the distortion of the first excited state along the ν(Fe−S) mode is substantially smaller for complex **2** than that for **1** (Δ = 2.1 and 3.3, respectively), while the corresponding distortions along the ν(Fe−Fe) modes are comparable in magnitude.

5. Excited-State Analysis. The excited-state nuclear distortions of complexes **1** and **2** were estimated using the following relationship between internal coordinate changes, Δr_i (Å), and dimensionless normal-coordinate displacements, Δ_k:[59]

$$\Delta r_i = 5.8065 \sum_k L_{i,k}(\Delta_k/\sqrt{\omega_k}) \qquad (2)$$

where $L_{i,k}$ is the ith element of the mass-weighted eigenvector, $\mathbf{L}_k$, for the kth normal mode ($\mathbf{L}_k$ was obtained from the NCAs discussed in section 3), and ω_k is the normal-mode frequency. The major molecular distortions of **1** in the first and third excited states are depicted in Figure 10.[60] Given the uncertainties in the Δ values determined from the experimental data,[58] the calculated distortions have errors in the range of 0.005−0.010 Å. These excited-state distortions are consistent with the TD-DFT-derived transition assignments provided above. For instance, transition i involves promotion of an electron into a MO (no. 96, Figure 6) that is strongly σ antibonding with respect to the Fe−Fe bond, thus accounting for the 0.19 Å elongation of the Fe−Fe bond in the first excited state.[61] Additionally, while the donor and acceptor orbitals associated with transition i are predominately Fe(I) d-orbital based (Table S2), they also contain a considerable degree of S 3p orbital character as revealed by the MO isosurface plots shown in Figure 8. Importantly, whereas the donor MO (no. 93) is bonding with respect to the four Fe−S bonds, the acceptor MO (LUMO, no. 96) is antibonding with respect to these bonds. Consequently, this transition is expected to result in sizable elongations of the Fe−S bonds, a prediction that concurs with the experimentally derived 0.08 Å increase in Fe−S bond lengths in the first excited state.

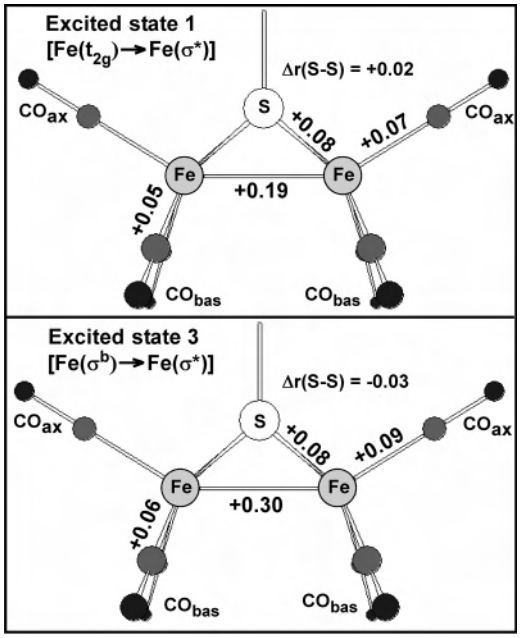

Figure 10. Experimentally derived distortions of complex **1** in excited states 1 and 3. Due to the (idealized) C_{2v} symmetry of the molecule, only one component of each type of symmetry-equivalent distortion is indicated.

The most dramatic molecular distortion experienced by complex **1** occurs in the third excited state, in which the Fe−Fe bond is elongated by 0.30 Å relative to the ground state. This result is fully consistent with the above assignment of transition $i\nu$ as possessing considerable Fe(σ^b) → Fe(σ^*) character, since such an excitation formally eliminates the bonding interaction between the two Fe(I) centers. As determined for the first excited state, in the third excited state, the Fe−S bonds likewise lengthen by 0.08 Å, again reflecting the Fe−S antibonding character of the LUMO. It is also important to note that, because of the electronic coupling between the Fe_2S_2 core and the carbonyl ligands, the Fe−C bonds experience moderate distortions in all excited states.

The corresponding analysis for complex **2** reveals similar excited-state geometries, displaying substantial elongations of 0.17 and 0.27 Å along the Fe−Fe bond axis in the first and third excited states, respectively (Figure S3). However, the Fe−S bond distances of **2** increase by a mere 0.045 Å in these excited states, which is significantly smaller than the 0.08 Å bond elongation calculated for **1** (Figure 10). Once again, this result reflects that $\Delta(\mathbf{1}) > \Delta(\mathbf{2})$ for the ν(Fe−S) modes (Table 5) and further corroborates our computational results. The reduction in Fe−S covalency upon dicyano substitution converting **1** to **2** leads to a decrease in thiolate contribution to the primarily Fe-based transitions that dominate the absorption spectra of the two models. As a result, on going from **1** to **2**, these transitions become more localized on the Fe(I)−Fe(I) core, thus greatly limiting changes in Fe−S bond distances in the latter complex.

Discussion

Implications for H_{red} State of FeHases. In recent years, synthetic chemists have made considerable progress in

(59) Myers, A. B.; Mathies, R. A. In *Biological Applications of Raman Spectroscopy*; Wiley: New York, 1987; Vol. 2, pp 1−58.
(60) Due to the assumption that $\Delta_{k,2} = \Delta_{k,3}$, the distortions in the second and third excited states are identical.
(61) The donor orbital for transition i is also Fe−Fe antibonding, but in a π fashion. As σ interactions are generally much stronger than π interactions, it is expected that this transition results in a net weakening of the Fe−Fe bond.

producing structural and functional models of the $[2Fe]_H$ component of the H cluster.[2,62] As these well-characterized synthetic complexes reasonably model the geometry and reactivity of the FeHase active site, they provide ideal systems through which to explore key electronic-structural features of the enzymatic system. In this study, we have explored the electronic structures of complexes **1** and **2** in detail, employing electronic absorption, MCD, and rR spectroscopies in conjunction with DFT and TD-DFT calculations. By combining the insights gained from our computational efforts with our spectroscopic results, we have succeeded in developing experimentally calibrated bonding descriptions for both complexes. These results have allowed for detailed assignments of the key features in the absorption spectra of **1** and **2** (Figures 7 and 8). Furthermore, analysis of the resonance de-enhancement observed in the rR excitation profiles has permitted us to elucidate the molecular distortions experienced by **1** and **2** in certain excited states (Figures 10 and S3). In this section, the possible implications of our results for the fully reduced ($\mathbf{H_{red}}$) state of the H cluster are explored.

By virtue of including both **1** and **2** in our combined spectroscopic/computational study, we have been able to examine the possible role of a mixed CO/CN ligation in promoting FeHase catalysis. Undoubtedly, the presence of anionic CN ligands tunes the redox potential of the active site, but our results suggest that it also alters the electronic structure in more subtle ways. Importantly, the bonding descriptions developed for **1** and **2** suggest that the Fe(I)−S bond covalency is significantly reduced upon dicyano substitution, while the remaining Fe(I)−CO π-backbonding interactions are enhanced, which likely contributes to the inability of **2** to bind additional CN ligands (vide supra). The fact that CN ligation modulates the nature of the Fe(I)−S bonds has important implications for the FeHase mechanism, as the thiolate ligands of the bridging pdt (or dta) moiety (Scheme 1) are proposed to function in proton shuttling to and from the active site.[13,22,63] By increasing the overall charge of the $[2Fe]_H$ component and producing more ionic Fe(I)−S bonds, CN ligation at the H cluster likely raises the pK_a of the thiolate ligands, thereby facilitating proton binding to the active site in the FeHase catalytic cycle.

A primary objective of this study has been to assess the potential of our computational methodology for providing viable electronic structure descriptions and spectral parameters. As demonstrated in the Results and Analysis section, DFT yields bonding descriptions of **1** and **2** that are fully consistent with our spectroscopic results, and furthermore, the TD-DFT calculated absorption spectra and transition assignments are in excellent agreement with our experimental absorption and MCD data. Consequently, we can confidently extend this computational methodology to the $\mathbf{H_{red}}$ state of the H cluster, for which only limited spectroscopic data are available. The $\mathbf{H_{red}}$ state is diamagnetic[12] and thus not amenable to study by EPR or MCD, and rR studies of $\mathbf{H_{red}}$ have only detected scattering from the conventional $[Fe_2S_2]$ and $[Fe_4S_4]$ clusters that are also present in FeHases.[64] Additionally, in all redox states, the absorption signal of the H cluster is obscured by the intense transitions of the other Fe−S clusters.[8] Therefore, computational methods are one of the few means available for the study of the $\mathbf{H_{red}}$ state.

Models of the $[2Fe]_H$ Subcluster. To test the validity of our computational methods for determining molecular structures, DFT geometry optimizations were performed on complexes **1** and **2** to yield models $\mathbf{1^{opt}}$ and $\mathbf{2^{opt}}$. As shown in Table S4, both optimized models are in good agreement with the corresponding experimental structures, although the Fe−Fe and Fe−S bond distances are slightly overestimated by 0.03−0.05 Å. The Fe−C distances are within 0.03 Å of the crystallographically determined values, and all bond angles agree to within 2°.[65] Thus, our computational methodology is clearly capable of providing reliable molecular structures for Fe(I) dimers with CO/CN ligation.

Geometry optimizations of the $[2Fe]_H$ component in the $\mathbf{H_{red}}$ state were performed using the X-ray crystal structure coordinates of the fully reduced H cluster from *D. desulfuricans* as the starting point[6] (see Experimental Section for computational details). Since the $[Fe_4S_4]$ component of the H cluster was not included in our calculations, the position of the bridging cysteine residue and proximal Fe (Fe_p) center were fixed to prevent structural changes incompatible with the constraints imposed by the protein backbone.[66] As in previous DFT studies of H cluster models,[13,67] calculations were performed with the cysteine residue in both its protonated and deprotonated forms, and the dithiolate unit was modeled as a neutral dta moiety.[68] Table 6 displays key structural parameters for the optimized models $\mathbf{[2Fe]_H\text{-}S}$ and $\mathbf{[2Fe]_H\text{-}SH}$. Although these two structures differ with respect to the protonation state of the terminal Cys residue, there are no major structural differences between the two models. Both geometries are in agreement with those obtained in previous computational studies of the $[2Fe]_H$ component,[13,69] and the calculated Fe−Fe bond distances of ∼2.6 Å are consistent with the crystallographic data.[6] In each model, the CO_b ligand occupies a semibridging position shifted

(62) Darensbourg, M. Y.; Lyon, E. J.; Zhao, X.; Georgakaki, I. P. *Proc. Natl. Acad. Sci. U.S.A.* **2003**, *100*, 3683−3688.
(63) Zhou, T. J.; Mo, Y. R.; Liu, A. M.; Zhou, Z. H.; Tsai, K. R. *Inorg. Chem.* **2004**, *43*, 923−930.
(64) (a) Fu, W.; Drozdzewski, P. M.; Morgan, T. V.; Mortenson, L. E.; Juszczak, A.; Adams, M. W. W.; He, S. H.; Peck, H. D.; Dervartanian, D. V.; Legall, J.; Johnson, M. K. *Biochemistry* **1993**, *32*, 4813−4819. (b) Macor, K. A.; Czernuszewicz, R. S.; Adams, M. W. W.; Spiro, T. G. *J. Biol. Chem.* **1987**, *262*, 9945−9947.
(65) The absorption spectrum of $\mathbf{1^{opt}}$ computed with TD-DFT (Figure S4) closely resembles that of **1**, indicating that, despite their small structural differences, the electronic structures of the two models are nearly identical. The most notable spectral change is the 1300 cm^{-1} red-shift of the dominant Fe(σ^b) → Fe(σ^*) transition in $\mathbf{1^{opt}}$ compared to **1**, a result of the longer Fe−Fe bond distance in the former model. For both models, the lower-energy shoulder has a computed energy of ∼23 100 cm^{-1}.
(66) The Fe−S_{Cys} bond distance was fixed at 2.35 Å, which is compatible with the distance of 2.38 Å found crystallographically.
(67) (a) Bruschi, M.; Fantucci, P.; De Gioia, L. *Inorg. Chem.* **2004**, *43*, 3733−3741. (b) Bruschi, M.; Fantucci, P.; De Gioia, L. *Inorg. Chem.* **2003**, *42*, 4773−4781.
(68) Geometry optimizations were also performed using the pdt ligand. The resulting structures were very similar to those obtained with a neutral dta ligand.
(69) Liu, Z. P.; Hu, P. *J. Am. Chem. Soc.* **2002**, *124*, 5175−5182.

Table 6. Structural Parameters and Fe Mulliken Charges of DFT-Optimized Models of the $[2Fe]_H$ Component of the H Cluster in the $\mathbf{H_{red}}$ State

model	$\mathbf{[2Fe]_H}$-S	$\mathbf{[2Fe]_H}$-SH
charge	−3	−2
	Structural parameters[a]	
r(Fe−Fe)	2.64	2.61
$r(Fe-S_b)_{ave}$[b]	2.36	2.35
$r(Fe_p-CO_b)$[c]	2.36	2.29
$r(Fe_d-CO_b)$[c]	1.78	1.78
$\Delta(Fe-CO_b)$[d]	0.58	0.51
$\angle(Fe_d-C-O)$[e]	154°	153°
	Mulliken charges	
Fe_p	−0.06	−0.12
Fe_d	−0.24	−0.23

[a] All bond lengths in Å. [b] Average of the four Fe−S bonds involving the bridging dta ligand. [c] Distance between Fe center and carbon atom of CO_b ligand. [d] Difference between $Fe_p-C(O)_b$ and $Fe_d-C(O)_b$ bond distances. [e] Angle between Fe_d-CO_b and intraligand bond vectors.

Scheme 3. MO Isosurface Plots for $\mathbf{H_{red}}$ Model $\mathbf{[2Fe]_H}$-S

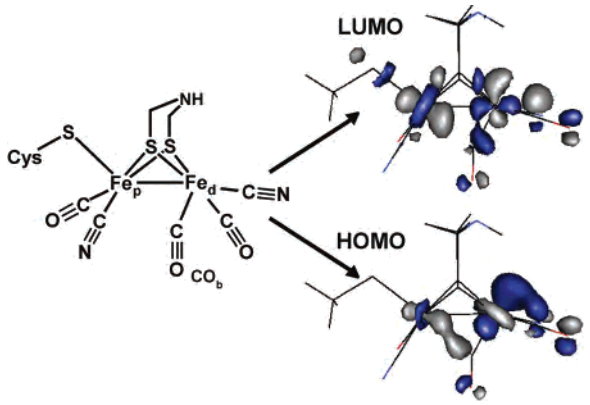

toward Fe_d, the difference between the two $Fe-C(O)_b$ bond lengths ($\Delta FeCO_b$) being 0.5−0.6 Å and the Fe_d-C-O bond angle amounting to 153° (Table 6). While this conformation does not appear to be entirely consistent with the crystallographic study of the $\mathbf{H_{red}}$ state of *D. desulfuricans*, which shows a fully terminal CO_b ligand ($\Delta FeCO_b$ = 0.7−0.9 Å and Fe_d-C-O bond angle of 176°),[6] a recent computational study has suggested that this crystal structure may actually be affected by protonation of the dta ligand.[69,70] Regardless, models $\mathbf{[2Fe]_H}$-S and $\mathbf{[2Fe]_H}$-SH adequately incorporate the most salient structural features of the $\mathbf{H_{red}}$ state, namely, the asymmetric position of CO_b beneath the Fe−Fe bond vector and a vacant coordination site on Fe_d.

Electronic Structure of $\mathbf{H_{red}}$ State. The MO bonding schemes that emerge from B3LYP DFT calculations on $\mathbf{[2Fe]_H}$-S and $\mathbf{[2Fe]_H}$-SH, while similar to one another, differ substantially from those developed for complexes **1** and **2**. Most significantly, the presence of the CO_b ligand prevents the formation of the strong Fe−Fe σ bond that exists in the synthetic models, and the HOMO and LUMO of $\mathbf{[2Fe]_H}$-S, shown in Scheme 3, bear little resemblance to the corresponding MOs of **1** and **2**. In fact, in relation to the synthetic models, the HOMO and LUMO of $\mathbf{[2Fe]_H}$-S are reversed in energy; for $\mathbf{H_{red}}$, the HOMO is now σ antibonding with respect to the Fe−Fe bond. This reversal is caused by the CO_b ligand, whose π^* orbital located in the $Fe_p-C(O)_b-Fe_d$ plane is favorably oriented to engage in bonding interactions with the Fe d_{z^2} orbitals, although the interaction with Fe_p is fairly weak because of the long $Fe_p-C(O)_b$ bond distance. As a result, the antibonding (σ^*) combination of Fe(d_{z^2}) orbitals is stabilized relative to the σ^b-based MO that consequently becomes the LUMO. This bonding pattern is essentially identical to that described by Liu et al.,[69] in which the redox-active MO of the $[2Fe]_H$ cluster was labeled "e_g-$2\pi(CO_b)$."

The asymmetric position of the CO_b ligand with respect to the two Fe centers also results in a considerable degree of charge localization within the redox active orbital, a phenomenon that has also been observed in DFT studies of FeHase model complexes.[21,62] Specifically, while the electron density in complexes **1** and **2** is distributed equally over the Fe centers (Tables S2 and S3), the Fe d-orbital character in the HOMOs of models $\mathbf{[2Fe]_H}$-S and $\mathbf{[2Fe]_H}$-SH is primarily located on Fe_d (Tables S7 and S8). This unequal electron distribution is also reflected in the relative Mulliken charges, which indicate that Fe_d is more negative than Fe_p in both models (Table 6). Collectively, these computational data suggest that the structure of the $[2Fe]_H$ cluster in the $\mathbf{H_{red}}$ state, in particular the semibridging (or terminal) position of the CO_b ligand, leads to a preferential localization of electron density on the Fe_d site, resulting in an electronic structure with considerable "$Fe_p(II)-Fe_d(0)$" character.

These results help elucidate the relationship between the geometric/electronic structures and the reactivity of the H cluster. As noted previously, Fe(I)−Fe(I) dimers, such as complex **3**, react with protons to form stable hydrido-bridged Fe(II)−Fe(II) dimers (Scheme 2). Similarly, in H_2-evolving hydrogenases, protons add to the H cluster $\mathbf{H_{red}}$ state in an oxidative addition step. Although no hydride-bound form of the H cluster has ever been isolated, an attractive possible role of the CO_b ligand is to shield the diiron unit from proton attack at the bridging position instead directing the proton to the vacant terminal position on Fe_d. Along with this steric role, the CO_b ligand also tunes the electronic structure of the $\mathbf{H_{red}}$ state so as to increase the nucleophilicity of the Fe_d center via the polarization of the electron density within the Fe−Fe bond. This is clearly evident in the HOMO of $\mathbf{[2Fe]_H}$-S (Scheme 3), which features a large lobe of electron density pointing toward the vacant coordination site of Fe_d, promoting proton binding at the terminal position.

TD-DFT Predicted Spectra. Prompted by its successful treatment of complexes **1** and **2**, the TD-DFT method using the B3LYP hybrid functional was also applied to model $\mathbf{[2Fe]_H}$-S. The computed absorption spectrum (Figure 11) exhibits two intense features ($\epsilon \approx 6000$ M^{-1} cm^{-1}) in the visible region at 17 300 and 20 000 cm^{-1}, labeled α and β, followed by a series of moderately intense bands ($\epsilon \approx 2000-6000$ M^{-1} cm^{-1}) between 22 000 and 32 000 cm^{-1}. Analysis of the TD-DFT results reveals that both transitions α and β possess primarily HOMO → LUMO character, while dif-

(70) Our DFT studies of $\mathbf{H_{red}}$ reproduce this shift in CO_b from a semibridging to a terminal position upon protonation of the dta ligand ($\Delta FeCO_b$ = 1.1 Å and $\angle$ (Fe_p-C-O) = 176°). In these structures, Fe forms a hydrogen bond with the N−H unit of dta, which appears to encourage the formation of a terminal CO_b conformation.

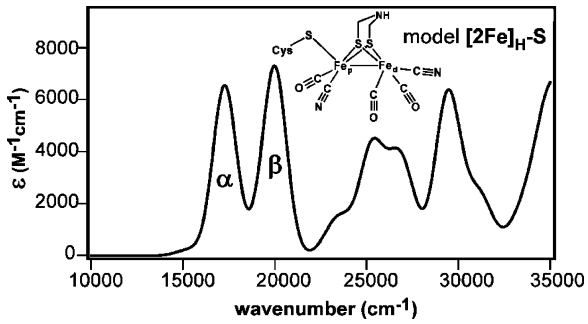

Figure 11. TD-DFT calculated absorption spectrum of the $[2Fe]_H$ subcluster model **$[2Fe]_H$-S**. Inset: Schematic representation of the structure of **$[2Fe]_H$-S**.

fering with respect to additional contributions from Fe d-based and $S_{Cys} \rightarrow$ Fe(I) CT excitations. The assignments are corroborated by the corresponding electron density difference maps (EDDMs), which provide a visual representation of the changes in electron density that occur upon excitation. The EDDMs for transitions α and β (Figure S5) indicate that both excitations are primarily centered on the Fe atoms, involving a considerable degree of electron transfer from Fe_d to Fe_p. Such intervalence transition character is consistent with the "Fe_p(II)−Fe_d(0)" formulation that emerged from the DFT calculations described above. The higher-energy bands in the near-UV region arise principally from Fe(t_{2g}) → LUMO transitions, and (as predicted for **1** and **2**) transitions above 32 000 cm^{-1} are due to Fe(I) d → CO π^* CT transitions.

Thus, although complex **2** and the $[2Fe]_H$ subcluster model **$[2Fe]_H$-S** have similar ligand sets and geometries, our computational results suggest that their electronic absorption spectra are quite distinct. For **2**, the dominant spectral features are found in the near-UV region, while all transitions in the visible region carry little absorption intensity. Alternatively, for the H cluster, this pattern seems reversed, with the most prominent feature(s) now appearing between 600 and 450 nm (16 700 and 22 200 cm^{-1}), while transitions in the near-UV region are somewhat less intense. This redistribution of absorption intensity between the two systems is a reflection of the differing bonding schemes presented above; namely, the partial disruption of the Fe−Fe bond by the semibridging CO_b ligand in the **$[2Fe]_H$-S** model reduces the HOMO/LUMO gap, red-shifting the intense Fe(I) e_g-based transition(s) into the visible region. Unfortunately, the strong absorption features associated with the conventional Fe−S clusters in FeHases prevent a direct comparison between our computed spectra and that of the $[2Fe]_H$ subcluster of the enzyme. Yet Pickett and co-workers have succeeded in trapping an Fe(I)−Fe(I) intermediate (**6**) at reduced temperatures that features a ligand set similar to that of model **$[2Fe]_H$-S**, including a (semi)bridging carbonyl moiety (Scheme 4).[71,72] When complex **5**, which is closely related to complex **2**, is converted into **6**, an intense absorption feature appears at 490 nm (20 400 cm^{-1}), while the dominant feature in the parent complex at 367 nm (20 800 cm^{-1}) loses nearly half

Scheme 4. Synthesis of Fe(I)−Fe(I) Complex with Bridging CO Ligand[71]

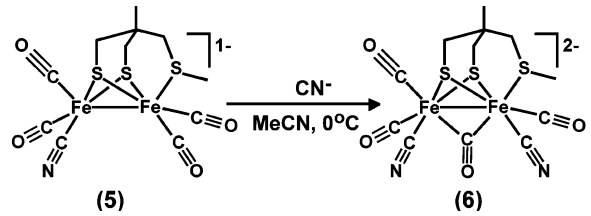

of its intensity (see Figure 7a in ref 66). The final absorption spectrum of intermediate **6** closely resembles the computed spectrum of the **$[2Fe]_H$-S** FeHase active-site model shown in Figure 11.[72] On the basis of these experimental observations and our computational predictions, we can speculate that the $[2Fe]_H$ component of the H cluster likely exhibits an absorption feature at ∼500 nm with an intensity of ∼5000−10 000 M^{-1} cm^{-1} due to Fe(I) d-based excitations.[73] This prediction should aid in the selection of suitable laser excitation wavelengths in future rR studies of FeHases.

Summary and Conclusions

The most significant findings of our combined spectroscopic/computational study of Fe(I)−Fe(I) dimer systems related to the H cluster are as follows:

(i) Analysis of our spectroscopic (rR) and computational (DFT) results indicate that the average Fe(I)−S bond covalency is significantly reduced upon dicyano substitution of **1** to generate **2**, while the remaining Fe(I)−CO π-back-bonding interactions are strengthened.

(ii) Time-dependent DFT (TD-DFT) provides calculated absorption spectra of **1** and **2** that agree nicely with the experimental absorption and MCD data, suggesting that this methodology is not limited to mononuclear transition-metal systems. On the basis of our TD-DFT results, the dominant bands at 30 400 and 28 100 cm^{-1} in the absorption spectra of **1** and **2**, respectively, are attributed to Fe(σ^b) → Fe(σ^*) transitions, while the lower-energy features for both complexes are assigned to Fe(t_{2g}) → Fe(σ^*) transitions.

(iii) The rR excitation profiles for **1** and **2** exhibit striking resonance de-enhancement due to destructive interference among multiple excited states. Simultaneous fitting of the rR excitation profiles and absorption spectra within the framework of time-dependent Heller theory reveals that, for both **1** and **2**, the Fe(σ^b) → Fe(σ^*) transition gives rise to a substantial elongation of the Fe−Fe bond by nearly 0.3 Å, thereby providing experimental evidence for a strong metal−metal bond in these dimers.

(iv) Application of the computational methodology used for complexes **1** and **2** to the fully reduced (**H_{red}**) state of the $[2Fe]_H$ subcluster provides clues as to the possible functional significance of this unique active-site structure. The CO_b ligand, which occupies a semibridging position in

(71) Razavet, M.; Davies, S. C.; Hughes, D. L.; Pickett, C. J. *Chem. Commun.* **2001**, 847−848.
(72) George, S. J.; Cui, Z.; Razavet, M.; Pickett, C. J. *Chem.—Eur. J.* **2002**, *8*, 4037−4046.
(73) In ref 72, the band at 490 nm was assigned to an Fe(I) → CO π^* CT transition. Our TD-DFT results indicate that such transitions occur at much higher energies, typically greater than 32 000 cm^{-1}.

our models, prevents the formation of a strong Fe(I)−Fe(I) σ bond as observed in the synthetic systems. Instead, the occupied MOs of the $\mathbf{H_{red}}$ model are preferentially localized on the Fe_d center, suggesting a "Fe_p(II)−Fe_d(0)" limiting description for this dimer. The resulting large lobe of electron density that points toward the vacant coordination site on Fe_d in the HOMO (Scheme 3) should greatly facilitate the oxidative addition of a proton to the H cluster in the catalytic cycle of the enzyme.

(v) TD-DFT calculations of our $\mathbf{H_{red}}$ model $\mathbf{[2Fe]_H}$**-S** suggest that, in contrast to **1** and **2**, the dominant spectral features of the $[2Fe]_H$ subcluster of FeHases appear in the visible region (650−450 nm). These transitions involve primarily HOMO → LUMO excitation and thus remain Fe d-based. Significantly, the computed absorption spectrum of model $\mathbf{[2Fe]_H}$**-S** closely resembles that published previously for an Fe(I)−Fe(I) complex possessing a bridging carbonyl ligand.[72] Thus, the presence of a terminal or semibridging CO ligand in the H cluster has an enormous effect on both the electronic and spectroscopic properties of the enzyme active site.

Acknowledgment. This research was supported by grants from the University of Wisconsin and the Sloan Foundation Research Fellowship Program (T.C.B.) and the NSF Graduate Research Fellowship Program (A.T.F.).

Supporting Information Available: Energies and compositions of relevant molecular orbitals from DFT calculations for complexes **1** and **2** (Tables S2 and S3, respectively) and models $\mathbf{[2Fe]_H}$**-S** and $\mathbf{[2Fe]_H}$**-SH** (Tables S7 and S8, respectively), Cartesian coordinates for DFT geometry-optimized models $\mathbf{1^{opt}}$, $\mathbf{2^{opt}}$, $\mathbf{[2Fe]_H}$**-S**, and $\mathbf{[2Fe]_H}$**-SH** (Tables S5 and S6), rR spectra of **1** and **2** obtained in MeCN solution (Figure S1), experimental and simulated absorption and rR excitation profile data for complex **2** (Figure S2), excited-state distortions of complex **2** (Figure S3), absorption spectrum of $\mathbf{1^{opt}}$ computed by TD-DFT (Figure S4), and electron density difference maps (EDDMs) calculated by TD-DFT for model $\mathbf{[2Fe]_H}$**-S** (Figure S5). This material is available free of charge via the Internet at http://pubs.acs.org.

IC048739N